International Journal of Solids and Structures 295 (2024) 112792

Contents lists available at ScienceDirect

International Journal of Solids and Structures

journal homepage: www.elsevier.com/locate/ijsolstr

An analytical study on SMA beam-column actuators for anti-buckling phenomenon

Alireza Ostadrahimi [a,*], Fathollah Taheri-Behrooz [b], Eunsoo Choi [c], Guoqiang Li [a]

[a] Department of Mechanical and Industrial Engineering, Louisiana State University, Baton Rouge, LA, USA
[b] School of Mechanical Engineering, Iran University of Science and Technology, Tehran, Iran
[c] Department of Civil Engineering, Hongik University, Seoul, South Korea

ARTICLE INFO

Keywords:
Anti-buckling
Shape memory alloy
Actuators
Beam-column

ABSTRACT

The present paper focuses on studying the anti-buckling behavior of prismatic martensitic shape memory alloy (SMA) beam-columns. It combines analytical and semi-analytical approaches to investigate the process of column straightening for anti-buckling. We try to comprehensively describe this phenomenon and develop a mathematical model to formulate each step of the anti-buckling problem. Due to the complex stress–strain behavior of SMA material, nine different stages of stress-height diagrams may potentially occur during this effect; thus, for facilitating the design process of SMA structures, corresponding forces and moments to each stage, are analytically derived. Our demonstration establishes that the primary cause of beam-column straightening is not the uniformity of stress, but rather the achievement of uniform strain across all fibers of the cross-section. This uniform strain distribution implies that the curvature of the beam-column diminishes to zero.

1. Introduction

Displacement (angle or stroke), load (or force) as well as bandwidth (frequency or speed) are three main technical objectives needing to be addressed in designing SMA actuators for any industrial application. There always exists a challenge between the constraints of a specific application or design and potentially satisfying its conflicting objectives based on their requirements. As an example, thicker actuators generate higher force but actuate more slowly than thinner ones, shorter length of actuators may require less triggering in energy, however, it provides less stroke or displacement. Moreover, environmental conditions, permissible weight and size, positional control and stability, cost, durability, and maintenance can be added to the available constraints (Billah et al., 2022; Fang, 2022; Rastjoo et al., 2020; Krishnaswamy et al., 2019; Choi et al., 2022).

In terms of motion, generally, SMA actuators might be classified into two types: translational (linear) motion as well as rotational (rotary) motion. In the first category, three designs may be introduced: one-directional (1D), antagonist, and bias-force actuators. Free recovery and constraint recovery which are mostly suitable for low-cycle and one-time applications can be considered for 1D actuators (Khalid et al., 2019; Arivanandhan et al., 2023; Lagoudas, 2008; Liu et al., 2023; Zhang et al., 2010). In biasing force actuators, mostly a preloaded spring can operate cyclically to quickly and frequently leave and return an SMA element to its permanent position. However, in an antagonistic approach, two SMA elements might be alternately actuated as activated (heated) and deactivated (cooled) devices (Kazemi and Jankowski, 2023; Richter et al., 2010; Kohl, 2004; Choi et al., 2021; Hartl et al., 2010; Shaw and Kyriakides, 1998).

According to extensive applications of SMA actuators, they may mechanically undergo various loading conditions and be manufactured in various configurations and shapes. However, compared with other loading types, axial and bending loadings may provide the most efficient energy density for SMA devices (Mohammad Hashemi et al., 2023; Li et al., 2023; Fahimi et al., 2019; Qian et al., 2022; Vahidi et al., 2021). Due to the promising performance of axial and bending loadings, various forms such as rods, beams, wires, tubes, helical springs, and ribbons are employed in most SMA applications (Mandal and Calladine, 2002; Do et al., 2023; Choi et al., 2022). Under such loading conditions, SMA actuators are potentially vulnerable to lose their stability and start buckling. However, these buckled SMA elements such as beams, or columns can be used in artificial muscles, energy harvesting, and bio-inspired robot applications when snapping from one state to another state by exciting with adequate input trigger (Kawate et al., 2018; Kohl

* Corresponding author.
E-mail address: aostad3@lsu.edu (A. Ostadrahimi).

https://doi.org/10.1016/j.ijsolstr.2024.112792
Received 13 July 2023; Received in revised form 3 March 2024; Accepted 25 March 2024
Available online 4 April 2024

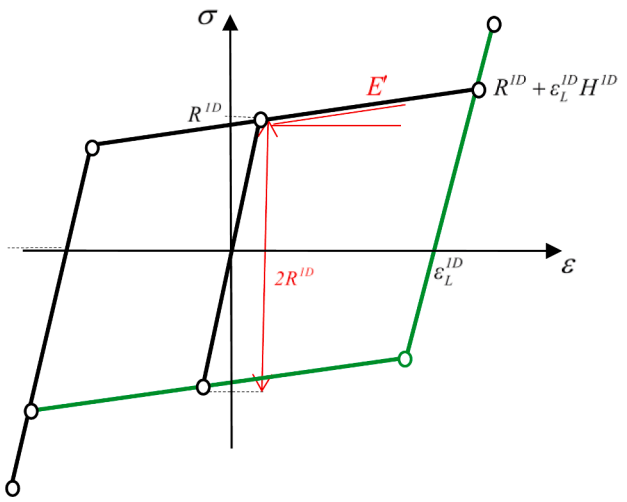

Fig. 1. The stress–strain characteristics and the material parameters associated with the Souza model (Ostadrahimi et al., 2015).

Table 1
Stress–strain relationship for different regions (Ostadrahimi et al., 2015).

Region Parameters	Elastic	Detwinning	Twined martensitic twin	Negative martensitic twin
Transformation strain (e^{tr})	0	$(\sigma-(R^{1D}+\tau_M^{1D}))/H^{1D}$	ε_L^{1D}	$-\varepsilon_L^{1D}$
Constitutive relation	$\sigma = E\varepsilon$	$\sigma = E'(\varepsilon+\varepsilon_0)$	$\sigma = E(\varepsilon-\varepsilon_L^{1D})$	$\sigma = E(\varepsilon+\varepsilon_L^{1D})$

et al., 2004; Choi et al., 2022; Tan et al., 2019). Thermal (or electrical) triggers are almost always a major activation method to induce phase transformation or detwinning process, whether an SMA element is embedded in a matrix or purely employed as a device or actuator for functional purposes (Choi et al., 2022; Tan et al., 2019; Das et al., 2021; Bovesecchi et al., 2019).

However, in this study, we have not used thermal or electrical stimuli; thus, athermally triggered SMA prismatic device to recover its original shape. In these forms of applications, a bent (or buckled) shape of an SMA element through twinning deformation effect (TD-Effect) which roots in an inhomogeneous stress state and then twined-detwinned variant orientation can be mechanically induced to recover inelastic strains (Richter et al., 2010; Urushiyama et al., 2003; Ostadrahimi et al., 2015; Zamani Alavije and Botshekanan Dehkordi, 2019; Thier et al., 1991; Watkins and Shaw, 2018). The TD-Effect was originally discovered and introduced by Urushiyama et al. (Urushiyama et al., 2003), who experimentally and numerically investigated the stress distribution and deformation of curved SMA columns under compression. Since in the curved shape of SMA elements, bending is the major mode of deformation; thus, via beam theory, several types of studies have been conducted to theoretically and experimentally obtain moment–curvature relationships for shape memory effect (SME) and superelastic (SE) beams and columns (Watkins and Shaw, 2018; Cheng et al., 2023; Xiao and Jiang, 2022; Jaber et al., 2008; Mirzaeifar et al., 2013; Rejzner et al., 2002; Ostadrahimi and Taheri-behrooz, 2019; Auricchio et al., 2011; Viet et al., 2019; Jiang et al., 2017; Viet et al., 2019; Karakalas and Lagoudas, 2020; Radi, 2021). Moreover, several buckling, unbuckling, and post-buckling analyses have been conducted to investigate the stability of columns with SME and SE before and after buckling or to postpone the instability of composites while SMA elements are embedded in them (Radi, 2021; Saeed Kamarian et al., 2020; Asadi et al., 2013; Pattar and Patil, 2019; Tung, 2017). By imposing initial pre-compression and using finite element analysis, Richter et al. (Richter et al., 2010) simulated anti-buckling analysis for SMA columns. Ostadrahimi et al. (Ostadrahimi and Taheri-behrooz, 2019) analytically solved the bending problem of pre-strained beams, however, their theory did not cover the TD-Effect and they roughly obtained the required force for strain recovery. Watkins et al. (Watkins and Shaw, 2018) using experimental and theoretical methods proved that unbuckling behavior for columns with SE may happen but only restricted to specific geometries and nonlinear material stress–strain curves.

The present paper is an analytical study on the anti-buckling of prismatic martensitic SMA beam-columns. The process of column straightening during anti-buckling is comprehensively described and based on that concept we mathematically modeled this physical phenomenon. In our analytical modeling, nine stages of loading and unloading stages during anti-buckling are step by step formulated, and the corresponding force and moment to each stage are derived and represented for designing purposes. To verify our modeling, we compare our results with existing numerical results. The structure of this paper is as follows. Section 2 is dedicated to the constitutive equation of SMA material. In section 3, which is the main section of this paper, the anti-buckling concepts are initially described and the moment–curvature relationship as well as stress analysis during the 9 stages are modeled. After deriving the deflection of the curved beam through semi-analytical methods, the results of this work have been presented in section 4 involving several numerical and experimental studies to address the anti-buckling phenomenon.

2. Reduced 1D Souza constitutive equations

The Souza model (Souza et al., 1998), developed in 1998, is a three-dimensional framework that effectively describes the unique effects of both pseudoelasticities (PE) and shape memory effect (SME) within the realm of small deformations. This model, rooted in the theory of irreversible thermodynamics, provides a general reduced one-dimensional representation when considering a uniaxial test. Inspired by the Souza Model (Souza et al., 1998) and then considering the reduced constitutive equations into one-dimensional form (Ostadrahimi et al., 2015), we have employed this model at low temperature or martensite phase, in line with the operating temperature of the TD-effect. Let σ,ε,E and e^{tr} be, respectively, the normal stress, strain, Elasticity modulus, and transformation strain, then

$$\sigma = E(\varepsilon - e^{tr}) \tag{1}$$

The stress–strain behavior of SMAs is indicated in Fig. 1 and their relationships for each region are proposed in Table 1.

Material parameters in the 1D Souza model (Fig. 1 and Table 1) can be described below:

$$\varepsilon_0 = \frac{R^{1D}+\tau_M^{1D}}{H^{1D}}, \quad E' = \frac{EH^{1D}}{H^{1D}+E}, \quad \varepsilon_L^{1D} = \left(\sqrt{2/3}\right)\varepsilon_L$$
$$H^{1D} = (3/2)H, \quad R^{1D} = \left(\sqrt{3/2}\right)R, \quad \tau_M^{1D} = \left(\sqrt{3/2}\right)\tau_M \tag{2}$$

where R,H and ε_L are, respectively, elastic domain radius, variant orientation hardening, and transformation strain at its maximum value during a uni-axial loading condition in a 3D model. Furthermore, considering T_0 and β reference temperature and a material parameter, respectively, τ_M may be defined as:

$$\tau_M = \begin{cases} \beta(T-T_0) & \text{if } T > T_0 \\ 0 & \text{otherwise} \end{cases} \tag{3}$$

3. Anti-buckling problem

In this section, we provide a concise description of the material behavior of SMA beam-column and its loading steps to display anti-buckling behavior. This problem consists of two stages: in the first

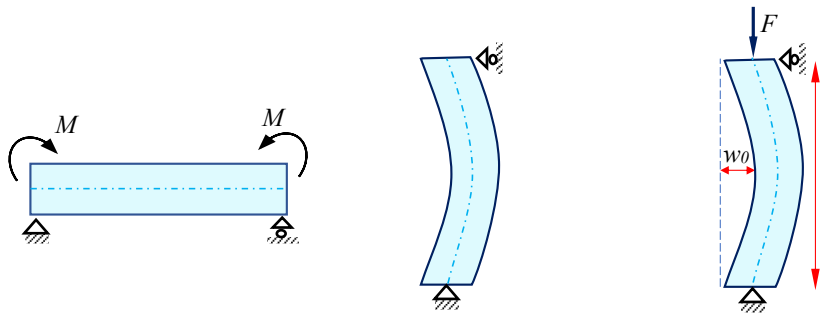

(a) Straight beam under bending stress (b) pre-bent beam (c) axial compression (anti-buckling effect)

Fig. 2. The process of loading stages to display the anti-bending problem.

Table 2
Maximum curvature and height of each one (Ostadrahimi et al., 2015).

Maximum elastic curvature	Maximum detwinning curvature	Height of elastic zone	Height of detwinning zone
$\kappa_e^{max} = \frac{2\sigma_s}{Eh}$	$\kappa_{de}^{max} = \frac{2}{h}\left(\frac{\sigma_f}{E} - \varepsilon_0\right)$	$h_e = \frac{\sigma_s}{E\kappa_l}$	$h_{de} = \frac{H^{1D}\varepsilon_L^{1D}}{E\kappa_l}$

stage, the pre-strained SMA beam undergoes bending stresses caused by transverse loading or bending moment (Fig. 2a). After removing the transverse load a residual deflection may remain in the beam. In the second stage, an axially compressive load exerts on this pre-bent beam; thus, in contrast to ordinary materials, beam deflection does not increase and/or buckle (Fig. 2b), rather the deflection starts decreasing and eventually it becomes straight (Fig. 2c).

Worth to note that when a martensite SMA beam is under bending stress, some fibers on both sides of the beam experience a detwinning process from twinned martensitic variants to positive or negative detwinned variants in tensile or compressive sides, respectively. By removing the transverse loads, a substantial deflection may remain in the beam-column and subsequently, bending stress distributes inhomogeneously across the cross-section. In the second stage as the axial load applies on the beam column, the fibers in the tensile side reorient into negative detwinned martensitic variants; thus, gradually a uniform stress distribution occurs in the beam meaning that residual curvature and deflection reach zero.

Since in the buckling and anti-buckling problem, geometry and length of columns play a crucial role, it is not expected for too long and aggressively bent SMA beam-columns to exhibit this TD-effect phenomenon. Thus, finding the exact range of length and degree of lateral deflection to exhibit anti-buckling behavior is important. For short columns, we may expect a higher possibility of having this effect due to the shear deformation effect; however, figuring out this exact range is under further investigation.

In the following discussion, we try to deeply describe the exact process of straightening in the beam and then analytically drive its governing equations to estimate the generated bending moment and required axial load as beam deflection reverts back to its initial shape. The pre-bent beam with length L and initial residual deflection will be exposed to a compressive load F as shown in Fig. 2c.

3.1. Stage I: Moment-curvature relationship for SMA beam-column under bending

In this section, to generate bending stress in the pseudo-plastic beam at the first stage, the bending moment–curvature relationship obtained by Ostadrahimi et al. (Ostadrahimi et al., 2015) is employed. In the most general stage, we can divide the cross-section into three zones, 1: elastic core when stress in these fibers is lower than detwinning start stress (σ_s), 2: detwinning zone when the fibers in this region have the stress in between σ_s and σ_f (detwinning finish stress), 3: saturation zone in which fibers are fully transformed to detwinned martensite. In order to obtain the total moment, bending moments in each region must be calculated and summed across the whole cross-section. The kinematics of a section may be described using two variables of normal strain (ε) and its corresponding curvature (κ). However, TD-effect may appear for short columns dominated by shear deformation, but due to the nonlinear behavior of SMA as well as intricated response of material during anti-buckling, for simplicity we have ignored the shear deformation term in this study, so normal strain varies linearly with the beam height (z).

$$\varepsilon(z) = -\kappa z \tag{4}$$

where let z be thickness of the beam-column as well. According to Table 1, the maximum elastic curvature (κ_e^{max}) and maximum detwinning curvature (κ_{de}^{max}) are obtained and presented in Table 2. For the curvature lower than κ_e^{max}, all fibers are located in the elastic zone, and for higher curvature, if some fibers exceed the detwinned zone, then the detwinning process should occur in the middle part (Fig. 3). To describe a complete bending moment–curvature relationship, it is necessary to obtain the boundaries of each zone (h_e and h_{de}, Fig. 3). Considering the normal strain at points a ($\varepsilon_a = \sigma_s/E$) and b ($\varepsilon_b = \sigma_s/E + H^{1D}\varepsilon_L^{1D}/E$) as well as Equation (4), the height of the elastic and detwinning zones are derived and presented in Table 2.

Let M, A and $t(z)$ be the bending moment, beam cross section area and thickness, respectively, the relationship between bending moment and curvature for this pseudo-plastic beam-column with prismatic cross-section may be given by $M = \int_A \sigma z\, t(z) dz$; thus, regarding Fig. 3 the most general stage of applied moment yields:

$$M_{loading} = 2\left(\int_0^{-h_e} E\varepsilon z\, t(z)dz + \int_{-h_e}^{-(h_e+h_{tr})} E'(\varepsilon+\varepsilon_0) z\, t(z)dz + \int_{-(h_e+h_{tr})}^{-h/2} E(\varepsilon - \varepsilon_L^{1D}) z\, t(z)dz\right) \tag{5}$$

Furthermore, the curvature can be calculated using $\kappa = d^2w/dx^2$ for the small lateral deflection (w). By integrating and then imposing suitable boundary conditions to find integration constants (C_1 and C_2), beam lateral deflection may be represented as

$$w(x) = \frac{\kappa x^2}{2} + C_1 x + C_2 \tag{6}$$

Upon unloading, some parts of martensite variants remain oriented while satisfying the equilibrium state and some parts may suffer from reorientation (Fig. 3b). However, reverse detwinning strain and stress may vary regarding the fibers' position (Ostadrahimi et al., 2015).

Based on the amount of applied bending load in this stage and then unloading, two possible diagrams of residual stress across the beam

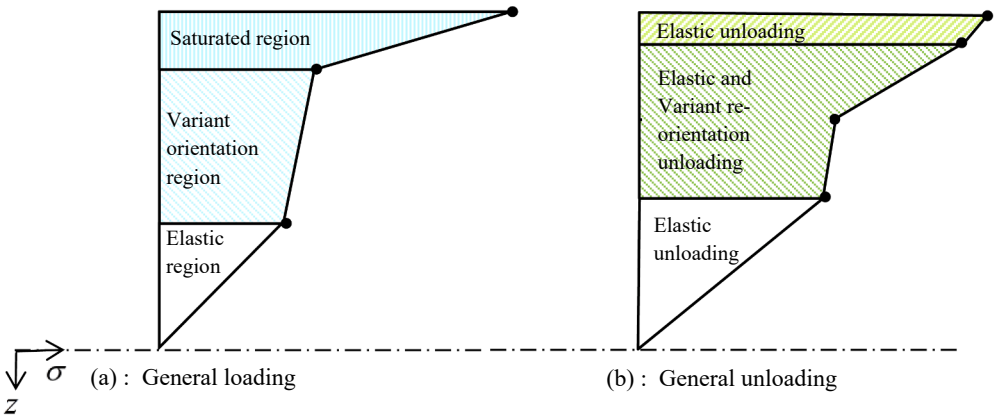

Fig. 3. Stress–strain diagram shows loading and unloading variations across regions (Ostadrahimi et al., 2015).

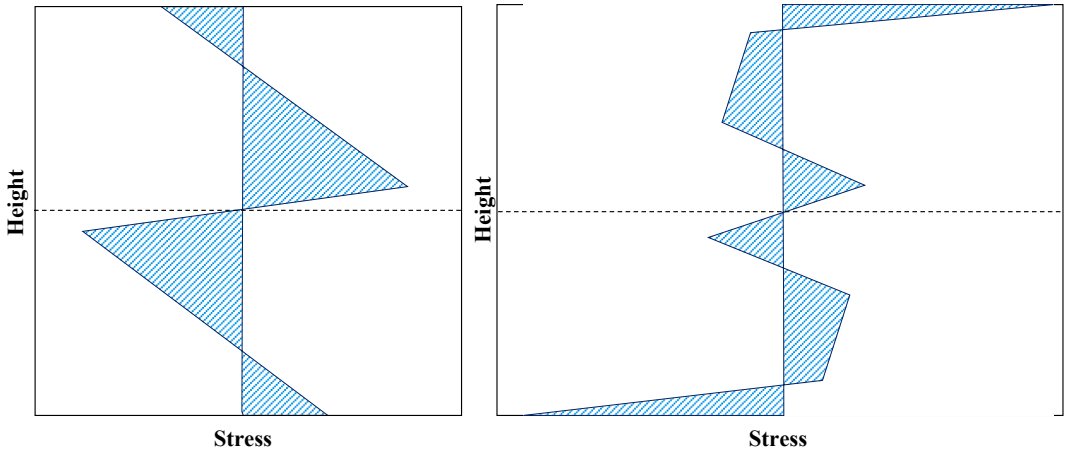

Fig. 4. Residual stress diagram upon unloading of bending load (Ostadrahimi et al., 2015).

cross-section can be formed (Fig. 4). Providing that during loading, the maximum induced stress in the outmost fiber of the beam does not exceed the detwinning finish stress (σ_F), the schematic of residual stress may follow Fig. 4a with three zero-stress fibers, otherwise the locked-in stress could develop in accordance with Fig. 4b exhibiting five neutral fibers.

3.2. *Stage II: Stress analysis of pre-bent column under axially compressive load*

In this section, an analytical solution is proposed to study governing equations of the anti-buckling effect, and then the relationships between force and moment with curvature and centroid residual strain are derived during each increment of loading. Furthermore, the process of beam straightening is investigated step by step, starting from an inhomogeneous stress diagram in Fig. 4 to reach uniform stress distribution while the curvature continuously reduces in 9 stages of stress profiles depicted in Fig. 5a and b. For more clarification, the circle symbol (○) is used in Fig. 5 to indicate the critical points of each stage during the loading procedure. As the fibers in the bending step experience detwinning and/or saturation regions, upon unloading, they may respectively reach the stress-height diagrams in Fig. 4a and b. For both residual stress diagrams in Fig. 4, the process of the anti-buckling effect would be the same. For simplicity, the deformed beam-column under the residual stress in Fig. 4a is considered. Stage 0 in Fig. 5a (⓪), exactly shows again the stress-height diagram of Fig. 4a, and the corresponding stress–strain curve to this stage, is shown in Fig. 6a by ⓪ again. Similarly, as another example, for stage 5 (*V*) in the stress-height diagram of Fig. 5b, the stress–strain distribution corresponding to this specific stage is illustrated by *V* in Fig. 6b. To clarify as to why both graphs in Fig. 4, may have similar process of TD-effect, we need to consider Figs. 4, 5, and 6 simultaneously. Overall, after unloading in bending step (shown by → for some points) and depending on fibers' location, fibers may stay in saturation region (bold line P1 to P2) and in stage 0 (P2 to P3 and P3 to P4) in Fig. 5a. Considering half of the beam, although the fibers at the end of unloading the second step are at different locations and regions (P1 to P4), upon exerting a compressive load at final step, all fibers based on their locations, initially experience a change of stress with the slop of E (same slop as unloading of bending step), and then reach their threshold of reverse detwinning (e.g. shown by $*$ for three pints), thus, the stress may vary by $E^{'}$ in the reverse detwinning region.

Therefore, regardless of the location of fibers either in the saturation region or in the detwinning region at the end of removing the bending step (Fig. 4a and b, respectively), the process of loading in final step may be similar in a way that it firstly goes toward the reverse detwinning region by slop of E, then upon reaching the reverse detwinning start stress (thresholds), their stress change may follow with the stiffness of $E^{'}$. This fact will be demonstrated in section 4.2 and Fig. 14, where, in spite of some fibers undergoing saturation region, the trends of stress-height diagram follow the procedure of stage *I* to *VIII*.

Upon exerting an axial load, the centroid strain (ε_g) starts emerging in the cross-section so that neutral fiber does not pass through the

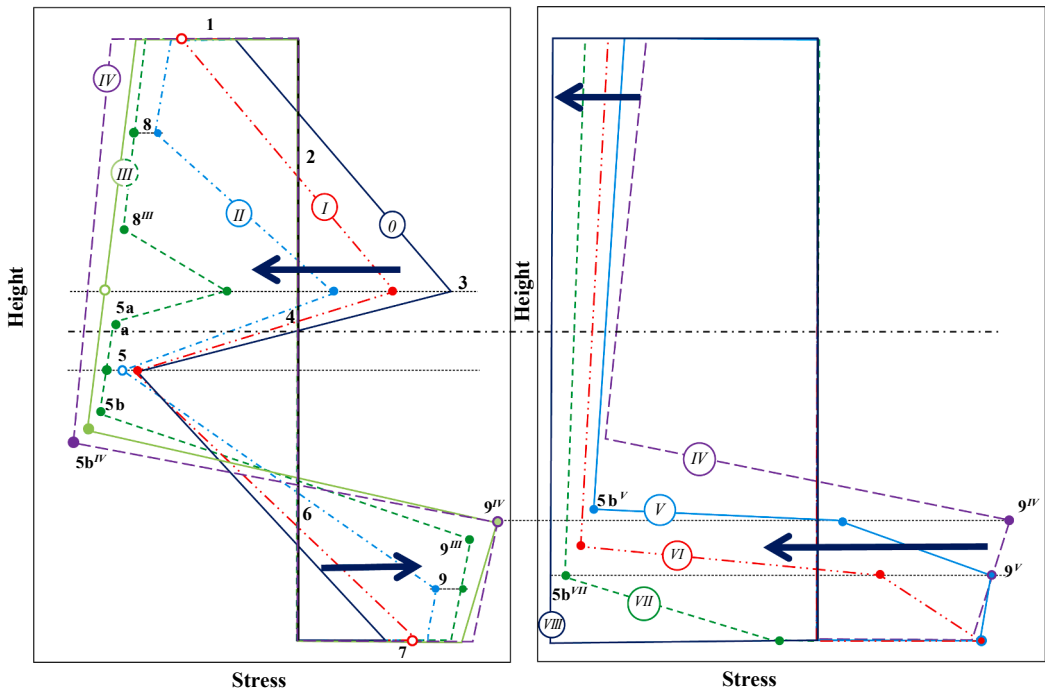

(a) Stages 0 to 4 (b) Stages 4 to 8

Fig. 5. History of stress-height diagram upon each stage of anti-buckling.

centerline; thus, equation (4) is no longer valid and the deformation profile should be modified as

$$\varepsilon(z) = -\kappa_l z + \varepsilon_g \tag{7}$$

where ε_g is a function of the applied load. To specify the normal stress changes for each fiber in the beam cross-section during each increment of loading, we first need to express the strain variation of a fiber ($\Delta\varepsilon_i$) in terms of decreased curvature ($\Delta\kappa$) and increased centroid strain ($\Delta\varepsilon_g$) for point i as

$$\Delta\varepsilon_i = -z_i\Delta\kappa + \Delta\varepsilon_g \tag{8}$$

Regarding Fig. 5a and b (stages *0* to *IX*) and employing Equations (8), we will try to derive the unknown parameters of heights and normal stresses of each stage in terms of reduced curvature and increased centroid strain. To discuss the anti-buckling procedure as clearly and concisely as possible, nine stages of Fig. 5a and b, are divided into sections *Stage 0 to II, Stage III to IV, and Stage V to IX*.

3.2.1. Stage 0 to II

After removing the applied bending loads at step 1, the internal bending moment becomes zero, and force equilibrium is satisfied by exerting no axial force. The residual stress profile (*stage 0* in Fig. 5) can be described as

$$\begin{aligned}
\sigma^{res}_{i(1,3)} &= -E^{'}(\kappa_l z_i - \varepsilon_0) - Ez_i\Delta^U\kappa \quad (a)\\
\sigma^{res}_{i(3,5)} &= -Ez_i(\kappa_l + \Delta^U\kappa) \quad (b)\\
\sigma^{res}_{i(5,7)} &= -E^{'}(\kappa_l z_i + \varepsilon_0) - Ez_i(\Delta^U\kappa) \quad (c)
\end{aligned} \tag{9}$$

where $\sigma^{res}_{i(1,3)}$ represents the remained stress in the fibers between points 1 and 3. Similarly, we can define the residual stresses of $\sigma^{res}_{i(3,5)}$ and $\sigma^{res}_{i(5,7)}$ for the fibers between points 3 to 5 and 5 to 7, respectively. $\Delta^U\kappa$ denotes the unloading reduced curvature and has been determined along with the height of points 3 and 5 (z_3,z_5) through the unloading step.

Upon exerting axially compressive load during *stage I*, all fibers initially undergo elastic stress variations ($\Delta\sigma = E\Delta\varepsilon$) which may have an increasing or decreasing trend based on their fiber's location. In this stage, the curvature reduces until the stress of the outmost fibers at points 1 (or 7) reaches the bound of the reverse detwinning region. To start the reverse detwinning process for points 1 to 3 (or 5 to 7), the total strain variation during unloading and *stage I* is $-2R/E$ ($\Delta^U\varepsilon + \Delta^I\varepsilon = -2R/E$); using Equations 8 and 9a; the increased centroid strain for the stage I ($\Delta^I\varepsilon_g$) can be written as

$$\Delta^I\varepsilon_g = -\left(\frac{2R}{E} - \frac{h(\Delta^U\kappa + \Delta^I\kappa)}{2}\right) \tag{10}$$

The initial centroid strain is zero ($\varepsilon^0_g = 0, \Delta^I\varepsilon_g = \varepsilon^I_g - \varepsilon^0_g$); thus, $\Delta^I\varepsilon_g$ could be equal to ε^I_g.

With the growth of the applied axial load, the beam curvature drops continuously, and as expected reverse detwinning process begins in some fibers from points 1 to 8 and 7 to 9 (Fig. 5a, *stage II*).

The internal force and bending moment for *stage II* may be written as

$$\begin{aligned}
F = -\Bigg(&\int_{-h/2}^{z_8}\sigma^{II}_{i(1,8)}t(z)dz + \int_{z_8}^{z_3}\sigma^{II}_{i(8,3)}t(z)dz + \int_{z_3}^{z_5}\sigma^{II}_{i(3,5)}t(z)dz + \int_{z_5}^{z_9}\sigma^{II}_{i(5,9)}t(z)dz\\
&+ \int_{z_9}^{h/2}\sigma^{II}_{i(9,7)}t(z)dz\Bigg) \quad (a)
\end{aligned} \tag{11}$$

$$\begin{aligned}
M = &\int_{-h/2}^{z_8}\sigma^{II}_{i(1,8)}zt(z)dz + \int_{z_8}^{z_3}\sigma^{II}_{i(8,3)}zt(z)dz + \int_{z_3}^{z_5}\sigma^{II}_{i(3,5)}zt(z)dz + \int_{z_5}^{z_9}\sigma^{II}_{i(5,9)}zt(z)dz\\
&+ \int_{z_9}^{h/2}\sigma^{II}_{i(9,7)}zt(z)dz \quad (b)
\end{aligned}$$

where and z_8, z_9 are unknown stress and height parameters, however, z_3 and z_5 are determined from the unloading stage. To derive $\sigma^{II}_{i(1,8)}$ and $\sigma^{II}_{i(9,7)}$, we know that the fibers located between points 1 to 8 (7 to 9) are expected to experience both elastic and reverse detwinning stress reduction; thus, employing Equation (8), the strain variation in this region decomposes into elastic ($\Delta^{II}\varepsilon^e$) and detwinning ($\Delta^{II}\varepsilon^d$) terms as

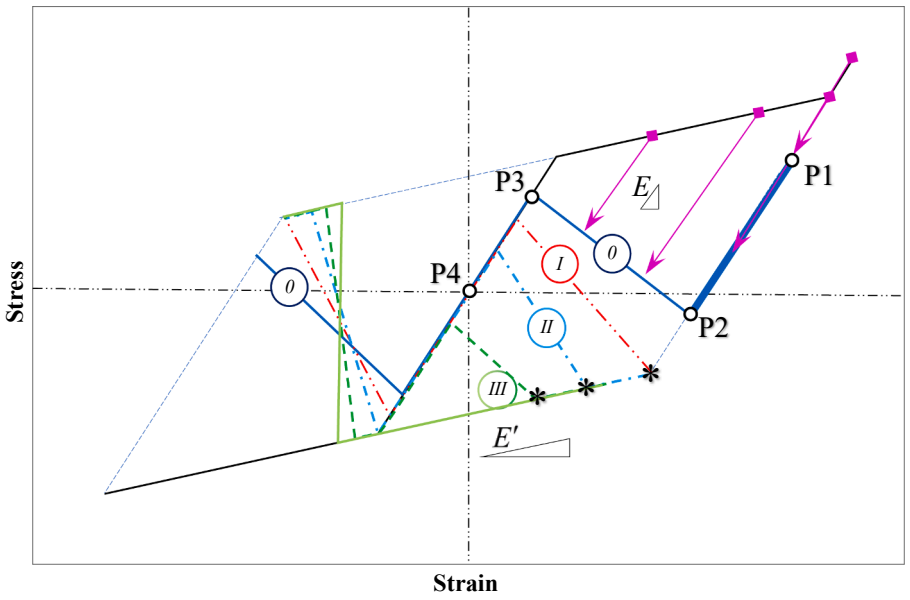

(a) Stages 0 to 3

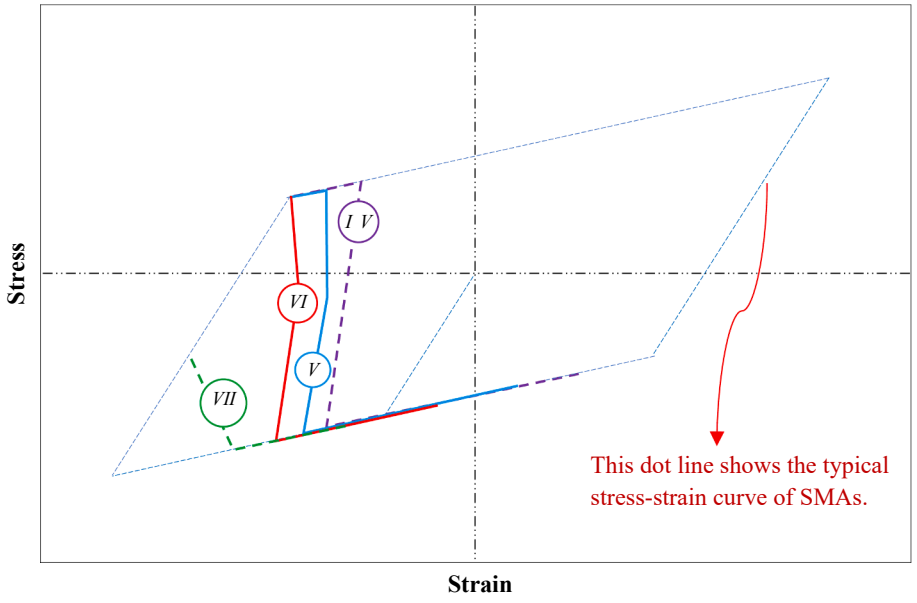

(b) Stages 4 to 7

Fig. 6. Residual stress–strain curves for each stage of anti-buckling.

$$\Delta^{II}\varepsilon = \Delta^{II}\varepsilon^{e} + \Delta^{II}\varepsilon^{d} \tag{12}$$

To derive the stress parameters of these regions for *stage II*, we can write

$$\begin{pmatrix} \sigma^{II}_{i(1,8)} = \sigma^{res}_{i(1,3)} \\ \sigma^{II}_{i(9,7)} = \sigma^{res}_{i(5,7)} \end{pmatrix} + E(\Delta^{I}\varepsilon + \Delta^{II}\varepsilon^{e}) + E^{'}\Delta^{II}\varepsilon^{d} \tag{13}$$

Regarding Fig. 6b, the elastic stress variation for the fibers between points 1 to 8 cannot exceed $-2R$ ($+2R$ for points 9 to 7); thus, $\Delta^{II}\varepsilon^{e}$ may be calculated as

$$\Delta^{II}\varepsilon^{e}_{i} = \begin{cases} -\left(\dfrac{2R}{E} + \Delta^{U}\varepsilon + \Delta^{I}\varepsilon\right) & 1 \le z \le 8 \\ \dfrac{2R}{E} - \left(\Delta^{U}\varepsilon + \Delta^{I}\varepsilon\right) & 9 \le z \le 7 \end{cases} \tag{14}$$

Substituting Equations (8), 12, and 14 into Equations (13), and after some mathematical manipulation $\sigma^{II}_{i(1,8)}$ and $\sigma^{II}_{i(9,7)}$ can be derived in terms of ε^{II}_{g} and $\Delta^{II}\kappa$ as

$$\begin{aligned} \sigma^{II}_{i(1,8)} &= -E^{'}z_i(\kappa_l + \Delta^{U}\kappa + \sum_{j=I}^{II}\Delta^{j}\kappa) + E^{'}(\varepsilon^{II}_{g} + \varepsilon_0) - 2R\left(1 - \frac{E^{'}}{E}\right) \\ \sigma^{II}_{i(9,7)} &= -E^{'}z_i(\kappa_l + \Delta^{U}\kappa + \sum_{j=I}^{II}\Delta^{j}\kappa) + E^{'}(\varepsilon^{II}_{g} - \varepsilon_0) + 2R\left(1 - \frac{E^{'}}{E}\right) \end{aligned} \tag{15}$$

For the fibers between points 8 to 3 and 3 to 5, the trend of stress variations is still purely elastic; $\sigma^{II}_{i} = \sigma^{res}_{i} + E\sum_{j=I}^{II}\Delta^{j}\varepsilon$; considering that $\sum_{j=I}^{II}\Delta^{j}\varepsilon_g = \varepsilon^{II}_{g}$, the locked-in stress for each zone yields

Table 3
Updated stress and height parameters for *Stages III* and *IV*.

$$\sigma^{III}_{i(1,8^{III})} = -E^{'}z_i(\kappa_l + \Delta^U\kappa + \sum_{j=I}^{III}\Delta^j\kappa) + E^{'}(\varepsilon_g^{III} - \varepsilon_0) - 2R\left(\frac{E^{'}}{E} - 1\right) \quad (a)$$

$$\sigma^{III}_{i(9^{III},7)} = -E^{'}z_i(\kappa_l + \Delta^U\kappa + \sum_{j=I}^{III}\Delta^j\kappa) + E^{'}(\varepsilon_g^{III} - \varepsilon_0) + 2R\left(\frac{E^{'}}{E} - 1\right) \quad (b)$$

$$\sigma^{III}_{i(8^{III},3)} = -E^{'}(\kappa_l z_i - \varepsilon_0) - Ez_i(\Delta^U\kappa + \sum_{j=I}^{III}\Delta^j\kappa) + E\varepsilon_g^{III} \quad (c)$$

$$\sigma^{III}_{i(3,5a)} = -Ez_i(\kappa_l + \Delta^U\kappa + \sum_{j=I}^{III}\Delta^j\kappa) + E\varepsilon_g^{III} \quad (d)$$

$$\sigma^{III}_{i(5b,O^{III})} = -E^{'}(\kappa_l z_i + \varepsilon_0) - Ez_i(\Delta^U\kappa + \Delta^I\kappa - \sum_{j=II}^{III}\Delta\kappa) + E(2\varepsilon_g^I - \varepsilon_g^{III}) \quad (e)$$

$$\sigma^{III}_{i(O^{III},9)} = -E^{'}(\kappa_l z_i + \varepsilon_0) - Ez_i(\Delta^U\kappa + \sum_{j=I}^{III}\Delta^j\kappa) + E\varepsilon_g^{III} \quad (f) \qquad (22)$$

$$\varepsilon_g^{III} = (\kappa_l + \Delta^U\kappa + \sum_{j=I}^{III}\Delta^j\kappa)\, z_3 - \frac{R}{E} \quad (23)$$

$$z_{8^{III}} = \frac{E\varepsilon_g^{III} + 2R}{E(\Delta^U\kappa + \sum_{j=I}^{III}\Delta^j\kappa)} \quad (a) \quad (24)$$

$$z_{9^{III}} = \frac{E\varepsilon_g^{III} - 2R}{E(\Delta^U\kappa + \sum_{j=I}^{III}\Delta^j\kappa)} \quad (b)$$

$$\sigma^{II}_{i(8,3)} = -E^{'}(\kappa_l z_i - \varepsilon_0) - Ez_i(\Delta^U\kappa + \sum_{j=I}^{II}\Delta^j\kappa) + E\varepsilon_g^{II} \quad (a)$$

$$\sigma^{II}_{i(3,5)} = -Ez_i(\kappa_l + \Delta^U\kappa + \sum_{j=I}^{II}\Delta^j\kappa) + E\varepsilon_g^{II} \quad (b) \qquad (16)$$

According to Equation (8), the fiber with zero strain variation is determined by $z_{O^{II}} = \Delta^{II}\varepsilon_g/\Delta^{II}\kappa$. This fiber successively relocates with each loading increment. Upon exerting axial load, it immediately departs from the centerline to the region between points 5 to 9. The fibers between points 5 to O^{II} and O^{II} to 9, subsequently suffer from negative and positive stress variations $\sigma^{res}_{i(5,7)} + E(\Delta^I\varepsilon \pm \Delta^{II}\varepsilon)$, respectively, therefore, the unknown parameter of $\sigma^{II}_{i(5,9)}$ consists of two terms as

$$\sigma^{II}_{i(5,O^{II})} = -E^{'}(\kappa_l z_i + \varepsilon_0) - Ez_i(\Delta^U\kappa + \Delta^I\kappa - \Delta^{II}\kappa) + E(2\varepsilon_g^I - \varepsilon_g^{II}) \quad (a)$$

$$\sigma^{II}_{i(O^{II},9)} = -E^{'}(\kappa_l z_i + \varepsilon_0) - Ez_i(\Delta^U\kappa + \sum_{j=I}^{II}\Delta^j\kappa) + E\varepsilon_g^{II} \quad (b) \qquad (17)$$

As mentioned earlier, to start the reverse detwinning process at point 8 (or 9), the totally reduced or increased stress is about $2R$; (the stress at points 8 and 9 reach $\sigma_{loading} \mp 2R$); therefore, using Equations 16a and 17b, respectively, the height of z_8 and z_9 can be written as

$$z_8 = \frac{E\varepsilon_g^{II} + 2R}{E(\Delta^U\kappa + \sum_{j=I}^{II}\Delta^j\kappa)} \qquad (18)$$

$$z_9 = \frac{E\varepsilon_g^{II} - 2R}{E(\Delta^U\kappa + \sum_{j=I}^{II}\Delta^j\kappa)} \qquad (19)$$

This form of stress distribution in stage *II* is valid until the stress at point 5 touches the detwinning start stress ($\sigma_s = -R$); so, employing Equation 16b, the critical condition at this state may be formulated as

$$\varepsilon_g^{II} = -\frac{R}{E} + z_5(\kappa + \Delta^U\kappa + \sum_{j=I}^{II}\Delta^j\kappa) \qquad (20)$$

Up to now, using Equations (10) and (18)-20, the internal force and moment for stages *I* and *II* may just be expressed in terms of unknown parameters of $\Delta^I\kappa$ and $\Delta^{II}\kappa$. For the abbreviation, we will derive the internal force and bending moment of the next stage (*II*) which could also cover stage *I*.

3.2.2. Stage III and IV

Due to the changes in the stress profile and trends of loading stress at *stage III*, the bending moment and internal force can be updated as

$$\begin{aligned} F &= -\left(\int_{-h/2}^{z_8^{IV}} \sigma^{III}_{i(1,8^{IV})}t(z)\,dz + \int_{z_8^{IV}}^{z_3} \sigma^{III}_{i(8^{IV},3)}\,t(z)\,dz + \int_{z_3}^{z_{5a}} \sigma^{III}_{i(3,5a)}\,t(z)\,dz \right. \\ &\quad + \int_{z_{5a}}^{z_{5b}} \sigma^{III}_{i(5a,5b)}\,t(z)\,dz + \int_{z_{5b}}^{z_9^{IV}} \sigma^{III}_{i(5b,9^{IV})}\,t(z)\,dz \\ &\quad \left. + \int_{z_9^{IV}}^{h/2} \sigma^{III}_{i(9^{IV},7)}\,t(z)\,dz\right) \quad (a)M \\ &= -\int_{-h/2}^{z_8^{IV}} \sigma^{III}_{i(1,8^{IV})}zt(z)\,dz + \int_{z_8^{IV}}^{z_3} \sigma^{III}_{i(8^{IV},3)}zt(z)\,dz + \int_{z_3}^{z_{5a}} \sigma^{III}_{i(3,5a)}zt(z)\,dz \\ &\quad + \int_{z_{5a}}^{z_{5b}} \sigma^{III}_{i(5a,5b)}zt(z)\,dz + \int_{z_{5b}}^{z_9^{IV}} \sigma^{III}_{i(5b,9^{IV})}zt(z)\,dz \\ &\quad + \int_{z_9^{IV}}^{h/2} \sigma^{III}_{i(9^{IV},7)}zt(z)\,dz \quad (b) \end{aligned} \qquad (21)$$

The unknown stress and height parameters of $\sigma^{III}_{i(1,8^{IV})}$,$\sigma^{III}_{i(9^{IV},7)}$,$\sigma^{III}_{i(8^{IV},3)}$,$\sigma^{III}_{i(3,5a)}$,$\sigma^{III}_{i(5b,9^{IV})}$,$z_8^{III}$ and z_9^{III} should be updated and unknown parameters of $\sigma^{III}_{i(5a,5b)}$,z_{5a} and z_{5b}^{III} must be derived in terms of reduced curvature.

In contrast to stage *II*, in the present stage stress distributions across points 1 to 8 (7 to 9), does not include elastic term and it is purely affected by detwinning process ($E^{'}\Delta^{III}\varepsilon$). However, for the fibers between points 8 to 8^{III} (9 to 9^{III}), both elastic and detwinning terms ($E^{'}\Delta^{III}\varepsilon^d + E\Delta^{III}\varepsilon^e$) become apparent; considering $\Delta^{III}\varepsilon^e + \Delta^U\varepsilon + \sum_I^{II}\Delta\varepsilon = -2R/E$, for points 1 to 8^{III}, ($=2R/E$for points 7 to 9^{III}) we write the updated stress parameters of these zones in Table 3. Similarly, the stress distributions along with the height of points $8^{'}$ to 5a and 5b to $9^{'}$ may be obtained in which $z_{O^{III}}$ can be determined by $z_{O^{III}} = \Delta^{III}\varepsilon_g/\Delta^{III}\kappa$. Furthermore, considering the stresses at points 8 and 9 ($\sigma_{loading} \mp 2R$) the parameters of $z_{8^{III}}$ and $z_{9^{III}}$ are updated in Table 3.

To derive $z_{5a^{III}}$ and $z_{5b^{III}}$, the normal stresses at points 5a and 5b may read, respectively, -*R* and $E^{'}(\varepsilon - \varepsilon_0)$ (the loading stresses at the first step); thus, using Equations 22d and 22e they can be expressed as

$$z_{5a^{III}} = \frac{E\varepsilon_g^{IV} + R}{E(\kappa + \Delta^U\kappa + \sum_{j=I}^{III}\Delta^j\kappa)} \quad (a)$$

$$z_{5b^{III}} = \frac{(2\varepsilon_g^I - \varepsilon_g^{III})}{(\Delta^U\kappa + \Delta^I\kappa - \sum_{II}^{III}\Delta^{II}\kappa)} \quad (b) \qquad (25)$$

Finally, in order to derive $\sigma^{III}_{i(5a,5b)}$, we know that when the stress at point 5 exceeds -*R*, the stress profile at this fiber does not vary elastically and variant orientation starts proceeding (5a to 5b at *stage III*); thus, the strain variations for these fibers consists of two terms including elastic

($\Delta^{III}\varepsilon^{e}$) and reverse detwinning process ($\Delta^{III}\varepsilon^{d}$). Due to the different loading stress of the fibers (points 5a to 5 and 5 to 5b), the stress profile in this region is diverse, so regarding Fig. 6b it yields

$$\sigma^{III}_{i(5a,5)} = E(\varepsilon + \Delta^{U}\varepsilon - \sum_{I}^{II}\Delta^{j}\varepsilon - \Delta^{III}\varepsilon^{e}) - E^{'}\Delta^{III}\varepsilon^{d} \quad (a) \tag{26}$$

$$\sigma^{III}_{i(5,5b)} = E^{'}(\varepsilon - \varepsilon_0 - \Delta^{III}\varepsilon^{d}) + E(\Delta^{U}\varepsilon - \sum_{j}^{II}\Delta^{j}\varepsilon - \Delta^{III}\varepsilon^{e}) \quad (b)$$

The fibers located between points 5a to 5b elastically revert to their initial loading position at the first stage; so the elastic strain reduction upon unloading ($\Delta^{U}\varepsilon$) is equal to the increased elastic strain of all stages:$\Delta^{III}\varepsilon^{e} = \Delta^{U}\varepsilon - \sum_{I}^{II}\Delta^{j}\varepsilon$; inserting this expression and Equation (8) into 26, the stress parameters may be derived in terms of ε^{III}_{g} and $\Delta^{III}\kappa$ as

$$\sigma^{III}_{i(5a,5)} = E^{'}z_i(\sum_{j=I}^{III}\Delta^{j}\kappa - \Delta^{U}\kappa) - E\kappa_l z - E^{'}\varepsilon^{III}_{g} \quad (a) \tag{27}$$

$$\sigma^{III}_{i(5,5b)} = -E^{'}z_i(\kappa_l + \Delta^{U}\kappa - \sum_{j=I}^{III}\Delta^{j}\kappa) - E^{'}(\varepsilon^{III}_{g} + \varepsilon_0) \quad (b)$$

where ε^{III}_{g} can be determined once the last fiber of the elastic region (point 3) meets the reverse detwinning process. This leads to the coincidence of points 8^{III}, and 5a with point 3 at the end of stage *III* while $\sigma^{III}_{i(3,5a)}$ becomes equal to $-R$; then substituting it into Equation 22d, ε^{III}_{g} is updated in Table 3 Note that, the growing trend of normal stress at point 9 for *stages II to IV*, shows that despite exerting axially compressive load, a significant number of fibers may be exposed to positive stress variation and subsequently suffer from the reverse detwinning process on the tensile side. However, this trend only last until the fiber with zero strain variation reaches point 9^{VI} ($z_{O^{IV}} = z_{9^{VI}}$). Updating Equation 24b for stage *IV* and assuming $z_{O^{IV}} = \Delta^{IV}\varepsilon_g/\Delta^{IV}\kappa$ the centroid strain at the end of this stage may be stated as

$$\varepsilon^{IV}_{g} = \frac{\left(\varepsilon^{III}_{g}(\Delta^{U}\kappa + \sum_{j=I}^{IV}\Delta^{j}\kappa) - \frac{2R}{E}\Delta^{IV}\kappa\right)}{\left(\Delta^{U}\kappa + \sum_{j=I}^{III}\Delta^{j}\kappa\right)} \tag{28}$$

Eventually, we could just express all unknown parameters in terms of $\Delta^{I}\kappa$ to $\Delta^{IV}\kappa$. Note that, by achieving stage *VI*, the stress variations may differ significantly so the corresponding equations must be derived and modified upon proceeding with axial load.

3.2.3. Stage V to VII

According to Fig. 5b, exerting more axial load causes the point with zero strain variation (O^{V}) gradually starts moving from point 9^{IV} toward 9^{V}. However, this fiber ends up reaching point 7 ($z = h/2$) in *stage VI*, and afterward, the whole fibers undergo negative stress variation ($\Delta\sigma < 0$). The more increase in the applied axial load (P), the more the stress reduction occurs in the fibers, eventually in stage *VII*, the beam has fully gone through the compressive region. To derive governing equations of this section, the general condition represented in *stage V* is considered; the corresponding internal force and bending moment may be stated as

$$F = -\left(\int_{-h/2}^{z^{VI}_{5b}}\sigma^{VI}_{i(1,5b^{VI})}t(z)\,dz + \int_{z^{VI}_{5b}}^{z^{V}_{9}}\sigma^{VI}_{i(5b^{VI},9^{VI})}\,t(z)\,dz + \int_{z^{V}_{9}}^{z^{VI}_{9}}\sigma^{VI}_{i(9^{V},9^{VI})}\,t(z)\,dz + \int_{z^{VI}_{9}}^{h/2}\sigma^{VI}_{i(9^{VI},7)}\,t(z)\,dz\right) \quad (a)$$

$$M = \int_{-h/2}^{z^{VI}_{5b}}\sigma^{VI}_{i(1,5b^{VI})}\,zt(z)\,dz + \int_{z^{VI}_{5b}}^{z^{V}_{9}}\sigma^{VI}_{i(5b^{VI},9^{VI})}\,zt(z)\,dz + \int_{z^{V}_{9}}^{z^{VI}_{9}}\sigma^{VI}_{i(9^{V},9^{VI})}\,zt(z)\,dz + \int_{z^{VI}_{9}}^{h/2}\sigma^{VI}_{i(9^{VI},7)}\,zt(z)\,dz \quad (b) \tag{29}$$

The unknown parameters of $\sigma^{V}_{i(1,5b^{V})}$,$\sigma^{V}_{i(9^{V},7)}$ and $z_{5b^{V}}$ should be updated and others stress parameters including $\sigma^{V}_{i(5b^{V},9^{IV})}$ and $\sigma^{V}_{i(9^{IV},9^{V})}$ must be derived following their new trends of loading.

The stress variation for the fibers between points 1 to $5b^{V}$, and 9^{V} to 7 is only caused by variant re-orientation in compressive and tensile sides, respectively. Hence, regarding the different loading histories arisen from previous stages (Equations 22d, 27a,b), and considering that for fibers between points 1 to 3 stress variation is $+E^{'}\Delta^{V}\varepsilon$ and for 3 to 5b seems $-E^{'}\Delta^{V}\varepsilon$;thus,$\sigma^{V}_{i(1,5b^{V})}$ can be obtained as

$$\sigma^{V}_{i(1,5b^{V})}: \begin{cases} \sigma^{V}_{i(1,3)} = -E^{'}z_i(\kappa_l + \Delta^{U}\kappa + \sum_{j=I}^{V}\Delta^{j}\kappa) + E^{'}(\varepsilon^{V}_{g} + \varepsilon_0) + 2R\left(\frac{E^{'}}{E} - 1\right) & (a) \\ \sigma^{V}_{i(3,5)} = E^{'}z_i(\sum_{j=I}^{V}\Delta^{j}\kappa - \Delta^{U}\kappa) - E\kappa_l z - E^{'}\varepsilon^{V}_{g} & (b) \\ \sigma^{V}_{i(5,5b^{V})} = -E^{'}z_i(\kappa_l + \Delta^{U}\kappa - \sum_{j=I}^{V}\Delta^{j}\kappa) - E^{'}(\varepsilon^{V}_{g} + \varepsilon_0) & (c) \end{cases} \tag{30}$$

When studying the stress of the fibers between points $5b^{V}$ to 9^{IV}, both elastic and reverse detwinning processes may occur in this region, using Equation 22f and $\Delta^{V}\varepsilon^{d} = \Delta^{V}\varepsilon - 2R/E$, $\sigma^{V}_{i(5b^{V},9^{V})}$ can be derived as

$$\sigma^{V}_{i(5b^{V},9^{IV})} = -E^{'}(\kappa_l z_i + \varepsilon_0 + \varepsilon^{V}_{g} - \varepsilon^{IV}_{g}) - Ez_i(\Delta^{U}\kappa + \sum_{j=I}^{IV}\Delta^{j}\kappa) + E\varepsilon^{IV}_{g} + E^{'}\Delta\kappa z + 2R\left(\frac{E^{'}}{E} - 1\right) \tag{31}$$

Stress variation induced in the fibers between points 9^{IV} to 9^{V} is purely elastic ($-E\Delta\varepsilon$), however, for points 9^{V} to 7 it is purely affected by detwinning process ($+E^{'}\Delta\varepsilon$). Employing Equation 22b, $\sigma^{V}_{i(9^{IV},9^{V})}$ and $\sigma^{V}_{i(9^{V},7)}$ can be expressed as

$$\sigma^{V}_{i(9^{IV},9^{V})} = -E^{'}z_i(\kappa_l + \Delta^{U}\kappa + \sum_{j=I}^{IV}\Delta^{j}\kappa - \frac{E}{E^{'}}\Delta^{V}\kappa) + E(\varepsilon^{V}_{g} - \varepsilon^{IV}_{g}) - 2R\left(\frac{E^{'}}{E} - 1\right) + E^{'}(\varepsilon^{IV}_{g} - \varepsilon_0)$$

$$\sigma^{V}_{i(9^{V},7)} = -E^{'}z_i(\kappa_l + \Delta^{U}\kappa + \sum_{j=I}^{V}\Delta^{j}\kappa) + E^{'}(\varepsilon^{V}_{g} - \varepsilon_0) - 2R\left(\frac{E^{'}}{E} - 1\right) \tag{32}$$

Finally, $z_{5b^{V}}$ can be determined by updating Equation 25b for *stage V*. Note that, at the end of this stage (Fig. 5b) the fiber with zero strain variation (O^{V}) reaches $z = h/2$, thus ε^{V}_{g} can be obtained as

$$\varepsilon^{V}_{g} = \varepsilon^{IV}_{g} + \frac{h}{2}\Delta^{V}\kappa \tag{33}$$

Furthermore, *stage VI* ends when point $5b^{VI}$ height becomes coincident with point 9^{V}; hence updating Equation (31) for *stage VI* and then employing Equations (33) and $z_{9^{V}} = \Delta^{V}\varepsilon_g/\Delta^{V}\kappa$, ε^{VI}_{g} maybe determined as

$$\varepsilon^{VI}_{g} = 2\varepsilon^{I}_{g} - \frac{h}{2}\left(\Delta^{U}\kappa + \Delta^{I}\kappa - \sum_{j=II}^{VI}\Delta^{j}\kappa\right) \tag{34}$$

After that, the stress variation trend follows *stage VII* and it lasts until

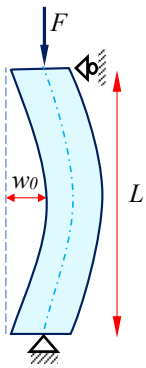

Fig. 7. A curved SMA beam under compressive force.

Table 4
Geometric and material parameters (Richter et al., 2010).

Geometric parameters	Value	Unit
t	4.38	mm
l	50	mm
h	4.38	mm
Material parameters		
M_S	44.6	°C
A_F	64.9	°C
ε_L^{1D}	4.4 %	–
E	30.9	GPa
E'	0	GPa
R^{1D}	290	MPa

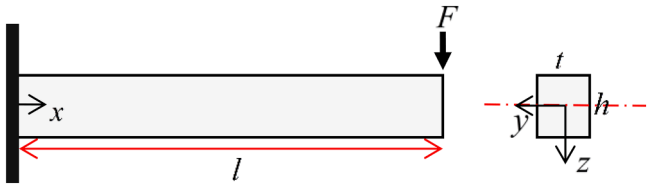

Fig. 8. A cantilever SMA beam subjected to a load perpendicular to its length.

eventually ε_g^{VII} reaches a specific value in the compressive region. Subsequently, stress distribution across the cross section turns out to be uniform and the column becomes straightened.

3.3. Deflection due to the anti-buckling properties

Due to the strong coupling of the TD-effect with the kinematics of short SMA beam-columns, the fully detwinned material response, notably stiffer than its twinned counterpart, facilitates late stiffening, enabling the beam-columns to self-straighten, a phenomenon unlike conventional plasticity relying on plastic lattice destruction (Richter et al., 2010). In the previous section, all unknown parameters related to each stage presented in Equations (11), 21, and 29 have been initially expressed in terms of reduced curvature ($\Delta\kappa$) and centroid strain (ε_g). Then employing the critical condition of each stage (Equations (10), 20, 23, 28, 33, and 34), we also derive ε_g in terms of reduced curvature, which contributes to expressing the internal forces and bending moment purely in terms of $\Delta\kappa$.

At any time during analysis, the internal force ($\int_A \sigma dA$) and externally applied load (F) must be equal and then by satisfying the equation of bending moment at the mid-span section we have:

$$\begin{aligned} &\int_A \sigma dA + F = 0 \qquad (a) \\ &M - F(w + w_0) = 0 \qquad (b) \end{aligned} \tag{35}$$

where M and w represent the internal bending moment ($\int_A \sigma z dA$) and transverse displacement, respectively. Moreover, w_0 in Fig. 7. denotes initial transverse displacement or residual deflection after the complete unloading of the bending moment in the first stage. Similar to column buckling and post-buckling problems, different theoretical approaches could be employed to provide an approximate solution for this problem. Pereira (Pereira, 2016) by considering the bending deflection profile, proposed an approximate but convenient solution to analyze the plastic buckling of columns. Motivated by this work, we employ the deflection-length relationship from the bending stage to investigate transverse displacement during the anti-buckling problem. For buckling and post-buckling analyses, the centroid strain cannot be determined so they used the Newton-Raphson method for re-establishing the equilibrium equations (Havran and Psotný, 2016; Carrera et al., 2021; Zhou et al., 2015). However, in this work, because we trace the changes of ε_g and obtain it in terms of $\Delta\kappa$, it is possible to explicitly obtain the relationship between force, moment, and residual deflection during each increment of loading. Although for better accuracy, upon applying compressive load the effect of beam shortening will be imposed by updating the beam length using $L_n^* = \varepsilon_{g_n} L_{n-1}^*$ (for $n = 1,\ldots m$).

Considering total reduced curvature ($\Delta\kappa_T = \sum \Delta\kappa_n$) just before reaching each stage and also simply supported boundary conditions in Equation (6), the deflection during each increment of loading at the middle of the beam can be stated as

$$w_n(l/2) = \left(\kappa + \Delta^U\kappa + \sum_1^m \Delta\kappa_n\right)\frac{L_n^{*2}}{8} \tag{36}$$

Substituting the internal force and bending moment of each stage (Equations (11), 21, and 29) as well as Equation (36) into Equation 35b, we can determine the maximum reduced curvature related to stages I to VII ($\Delta^i\kappa_{max}, i = I - VII$). Regarding the derived equations of each stage (f, M, and ε_g) in section 5, $\Delta\kappa$ is increased from zero, and then upon reaching $\Delta^i\kappa_{max}$ of each stage, the corresponding equations to the next stage will be employed during curvature reduction; thus, this process continues until $\Delta\kappa_T$ meets $\kappa - \Delta^U\kappa$ meaning that the pre-bent beam is straightened when the axially compressive load is applied during anti-bending analysis.

4. Results

In this section, several anti-buckling stage studies under different loading and geometric conditions are presented and then compared with existing numerical models. Initially, the relationship between load and deflection during loading and unloading in the bending section is studied, then for the anti-buckling problem the relationship between column length and transverse displacement upon strain recovery is extracted. Moreover, in this section, for deeper physical understanding the stress and strain distributions during anti-buckling of the SMA beam-columns are depicted.

4.1. Example 1

In this example, the anti-buckling problem reported by Richter et al. (Richter et al., 2010) under trigonometric loading is analytically solved and then compared with the numerical results. A cantilever SMA column with material parameters presented in Table 4 and geometric parameters of height h; length l, and width t under an applied load P (Fig. 8) at the free end are considered. Comparing the material behavior and parameters of SMA in reference (Richter et al., 2010) with the material parameters of Eq. (2) in the present work, it can be figured out that the hardening parameter in (Richter et al., 2010), equivalent to H^{1D} in this work, has not been considered. Thus, according to Eq.2, E' may obtain zero. Moreover, in the present study, R^{1D} introduces the radius of elastic domain, this parameter in the reference (Richter et al., 2010) is defined

Table 5
Corresponding internal force and bending moment of each anti-buckling stage.

Stage		Internal Force and Bending Moment
	F	$\frac{1}{2}\left[\sigma_1\left(\frac{h}{2}+z_2\right)+\sigma_3(z_4-z_2)+\sigma_5(z_6-z_4)+\sigma_7\left(\frac{h}{2}-z_6\right)\right]$
I	*M*	$\frac{\sigma_P}{2}z_5^2+\frac{(\sigma_5-\sigma_P)}{3}\frac{z_5^2}{3}+\frac{\sigma_5}{2}(z_6-z_5)\left(\frac{2}{3}z_5+\frac{z_6}{3}\right)+\frac{\sigma_7}{6}\left(\frac{h}{2}-z_6\right)(h+z_6)-$ $\left(\frac{\sigma_1}{6}\left(\frac{h}{2}-z_2\right)(h+z_2)+\frac{\sigma_3}{2}(z_3-z_2)\left(-\frac{2}{3}z_3-\frac{z_2}{3}\right)+\frac{\sigma_3}{2}(z_4-z_3)\left(-\frac{2}{3}z_3-\frac{z_4}{3}\right)+-\frac{\sigma_P}{6}z_4^2\right)$
	F	$\frac{1}{2}\left[(\sigma_1+\sigma_8)\left(\frac{h}{2}+z_8\right)+\sigma_3(z_4-z_2)+\sigma_5(z_6-z_4)+(\sigma_7+\sigma_9)\left(\frac{h}{2}-z_9\right)\right.$ $\left.-\sigma_8(z_8-z_2)+\sigma_9(z_9-z_6)\right]$
II	*M*	$\frac{\sigma_P}{2}z_5^2+\frac{(\sigma_5-\sigma_P)}{3}\frac{z_5^2}{3}+\frac{\sigma_5}{2}(z_6-z_5)\left(\frac{2}{3}z_5+\frac{z_6}{3}\right)+\frac{\sigma_9}{2}(z_9-z_6)\left(\frac{2}{3}z_9+\frac{z_6}{3}\right)+$ $\frac{\sigma_7}{2}\left(\frac{h^2}{4}-z_9^2\right)+\frac{(\sigma_9-\sigma_7)}{6}\left(\frac{h}{2}-z_9\right)\left(\frac{h}{2}+2z_9\right)-$ $\left(\frac{\sigma_1}{2}\left(\frac{h^2}{4}-z_8^2\right)+\frac{(\sigma_8-\sigma_1)}{6}\left(\frac{h}{2}+z_8\right)\left(\frac{h}{2}-2z_8\right)-\frac{\sigma_8}{2}(z_2-z_8)\left(-\frac{2}{3}z_8-\frac{z_2}{3}\right)+\right.$ $\left.\frac{\sigma_3}{2}(z_3-z_2)\left(-\frac{2}{3}z_3-\frac{z_2}{3}\right)+\frac{\sigma_3}{2}(z_4-z_3)\left(-\frac{2}{3}z_3-\frac{z_4}{3}\right)+-\frac{\sigma_P}{6}z_4^2\right)$
	F	$\frac{1}{2}\left[(\sigma_1+\sigma_8)\left(\frac{h}{2}+z_8\right)+\sigma_3(z_4-z_2)+\sigma_{5a}(z_{5a}-z_4)+(\sigma_{5a}+\sigma_{5b})(z_{5b}-z_{5a})+\right.$ $\left.\sigma_{5b}(z_6-z_{5b})+(\sigma_7+\sigma_9)\left(\frac{h}{2}-z_9\right)+\sigma_8(z_2-z_8)+\sigma_9(z_9-z_6)\right]$
III	*M*	$\frac{\sigma_P}{2}z_{5a}^2+(\sigma_{5a}-\sigma_P)\frac{z_{5a}^2}{3}+\frac{\sigma_{5a}}{2}(z_{5b}-z_{5a})\left(z_{5b}-\frac{z_{5a}}{2}\right)+\frac{(\sigma_{5b}-\sigma_{5a})}{2}(z_{5b}-z_{5a})\left(\frac{2}{3}z_{5b}+\frac{z_{5a}}{3}\right)+$ $\frac{\sigma_{5b}}{2}(z_6-z_{5b})\left(\frac{2}{3}z_{5b}+\frac{z_6}{3}\right)+\frac{\sigma_9}{2}(z_9-z_6)\left(\frac{2}{3}z_9+\frac{z_6}{3}\right)+\frac{\sigma_7}{2}\left(\frac{h^2}{4}-z_9^2\right)-$ $\left(\frac{(\sigma_8-\sigma_1)}{6}\left(\frac{h}{2}+z_8\right)\left(\frac{h}{2}-2z_8\right)-\frac{(\sigma_9-\sigma_7)}{6}\left(\frac{h}{2}-z_9\right)\left(\frac{h}{2}+2z_9\right)+\frac{\sigma_8}{2}(z_2-z_8)\left(-\frac{2}{3}z_8-\frac{z_2}{3}\right)+\right.$ $\left.\frac{\sigma_1}{2}\left(\frac{h^2}{4}-z_8^2\right)+\frac{\sigma_3}{2}(z_3-z_2)\left(-\frac{2}{3}z_3-\frac{z_2}{3}\right)+\frac{\sigma_3}{2}(z_4-z_3)\left(-\frac{2}{3}z_3-\frac{z_4}{3}\right)+\frac{\sigma_P}{6}z_4^2\right)$
	F	$\frac{1}{2}\left[(\sigma_1+\sigma_8)\left(\frac{h}{2}+z_8\right)+(\sigma_3+\sigma_8)(z_3-z_8)+(\sigma_{5a}+\sigma_3)(z_{5a}-z_3)+(\sigma_{5a}+\sigma_{5b})(z_{5b}-z_{5a})\right.$ $\left.+\sigma_{5b}(z_6-z_{5b})+(\sigma_7+\sigma_9)\left(\frac{h}{2}-z_9\right)+\sigma_8(z_2-z_8)+\sigma_9(z_9-z_6)\right]$
IV	*M*	$-\frac{\sigma_1}{8}h^2-\frac{(\sigma_P-\sigma_1)}{24}h^2+\frac{\sigma_P}{2}z_{5b}^2+(\sigma_{5b}-\sigma_P)\frac{z_{5b}^2}{3}+\frac{\sigma_{5b}}{6}(z_6-z_{5b})(z_6-2z_{5b})+$ $\frac{\sigma_9}{6}(z_9-z_6)(2z_9+z_6)+\frac{\sigma_7}{2}\left(\frac{h^2}{4}-z_9^2\right)+\frac{(\sigma_9-\sigma_7)}{6}\left(\frac{h}{2}-z_9\right)\left(\frac{h}{2}+2z_9\right)$
	F	$\frac{1}{2}\left[(\sigma_1+\sigma_{5b})\left(\frac{h}{2}+z_{5b}\right)+\sigma_{5b}(z_6-z_{5b})+\sigma_{9^{IV}}(z_{9^{IV}}-z_6)+(\sigma_{9^{IV}}+\sigma_{9^V})(z_{9^V}-z_{9^{IV}})\right.$ $\left.+(\sigma_7+\sigma_{9^V})\left(\frac{h}{2}-z_{9^V}\right)\right]$
V	*M*	$-\frac{\sigma_1}{8}h^2-\frac{(\sigma_P-\sigma_1)}{24}h^2+\frac{\sigma_P}{2}z_{5b}^2+(\sigma_{5b}-\sigma_P)\frac{z_{5b}^2}{3}+\frac{\sigma_{5b}}{6}(z_6-z_{5b})(z_6-2z_{5b})+$ $\frac{\sigma_{9^{IV}}}{6}(z_{9^{IV}}-z_6)(2z_{9^{IV}}+z_6)+\frac{(\sigma_{9^V}-\sigma_7)}{6}\left(\frac{h}{2}-z_{9^V}\right)\left(\frac{h}{2}+2z_{9^V}\right)+\frac{\sigma_7}{2}\left(\frac{h^2}{4}-z_{9^V}^2\right)+$ $\frac{(\sigma_{9^V}-\sigma_{9^{IV}})}{6}(z_{9^V}-z_{9^{IV}})(2z_{9^V}+z_{9^V})+\frac{\sigma_{9^{IV}}}{2}\left(z_{9^V}^2-z_{9^{IV}}^2\right)$
	F	$\frac{1}{2}\left[(\sigma_1+\sigma_{5b})\left(\frac{h}{2}+z_{5b}\right)+\sigma_{5b}(z_6-z_{5b})+\sigma_{9^V}(z_{9^V}-z_6)+(\sigma_7+\sigma_{9^V})\left(\frac{h}{2}-z_{9^V}\right)\right]$
VI	*M*	$-\frac{\sigma_1}{8}h^2-\frac{(\sigma_P-\sigma_1)}{24}h^2+\frac{\sigma_P}{2}z_{5b}^2+(\sigma_{5b}-\sigma_P)\frac{z_{5b}^2}{3}+\frac{\sigma_{5b}}{6}(z_6-z_{5b})(z_6-2z_{5b})+$ $\frac{\sigma_{9^V}}{6}(z_{9^V}-z_6)(2z_{9^V}+z_6)+\frac{\sigma_{9^V}}{2}\left(\frac{h^2}{4}-z_{9^V}^2\right)+\frac{(\sigma_7-\sigma_{9^V})}{6}\left(\frac{h}{2}-z_{9^V}\right)(h+z_{9^V})$
	F	$\frac{1}{2}\left[(\sigma_1+\sigma_{5b^{VII}})\left(\frac{h}{2}+z_{5b^{VII}}\right)+(\sigma_7+\sigma_{5b^{VII}})\left(\frac{h}{2}-z_{5b^{VII}}\right)\right]$
VII	*M*	$-\frac{\sigma_1}{8}h^2-\frac{(\sigma_P-\sigma_1)}{24}h^2+\frac{\sigma_P}{2}z_{5b^{VII}}^2+(\sigma_{5b^{VII}}-\sigma_P)\frac{z_{5b^{VII}}^2}{3}+\frac{\sigma_7}{2}\left(\frac{h^2}{4}-z_{5b^{VII}}^2\right)$ $+\frac{(\sigma_7-\sigma_{5b^{VII}})}{6}\left(\frac{h}{2}-z_{5b^{VII}}\right)\left(\frac{h}{2}+2z_{5b^{VII}}\right)$
VIII	*F*	$\sigma_1 h$
	M	0

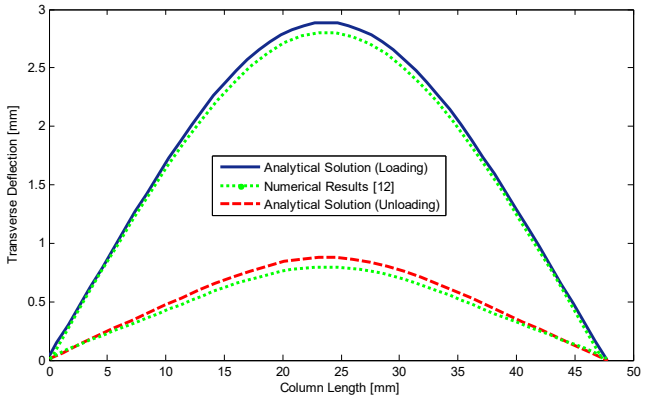

Fig. 9. Comparing variations in transverse deflection along the column length. Results of this work vs. existing numerical data (Richter et al., 2010).

as *"the positive transformation stress plateau"* with a value of 290 MPa. Respectively, ε_L^{1D} and E in this study, are equivalent to ε_T and E_M which are "*Transformation strain of martensite*" and "*Youngs modulus of martensite*" in (Richter et al., 2010). According to sections 3.2.1 to 3.2.3 the internal forces and bending moments for *Stage I* to *Stage VIII* are obtained and summarized in Table 5.

Employing the bending equations, the relationship between the length and deflection of the SMA beam-column during loading and unloading are compared in Fig. 9. It is important to highlight that, in order to report the beam deflection referenced in (Richter et al., 2010), we have digitized the deflections of the SMA beam along its length at the corresponding times of 25 s and 30 s in (Richter et al., 2010) for the loading and unloading processes, respectively.

In terms of strain and stress distribution in fibers, Fig. 10 shows the strain–stress distribution of all fibers for the cross section at the middle length of the beam. The numbers in the figure sequentially show the state of stress and strain variations for all three stages of loadings. At the end of each step, we put a mark to distinguish the steps. Due to the uniform stress distribution of the first step, all fibers have the same amount of stress, thus, in the figure all fibers are coincident on only one solid path (1 to 3: loading, and 3 to 4: unloading to end up at zero stress). However, due to non-uniform bending stress distribution, we may have divergence of fibers upon unloading, the solid path 5 forks off right, e.g. path 6 which finally stops on black square ■. Eventually, all diverged fibers (e.g. path 7) will be converged again following 8, and by removing

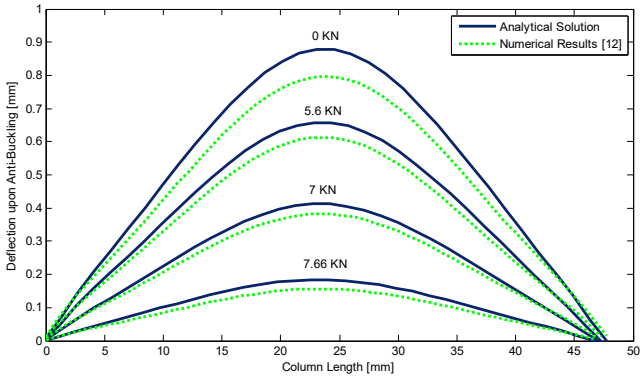

Fig. 11. Analytical solution and numerical results for deflection due to anti-buckling as a function of column length.

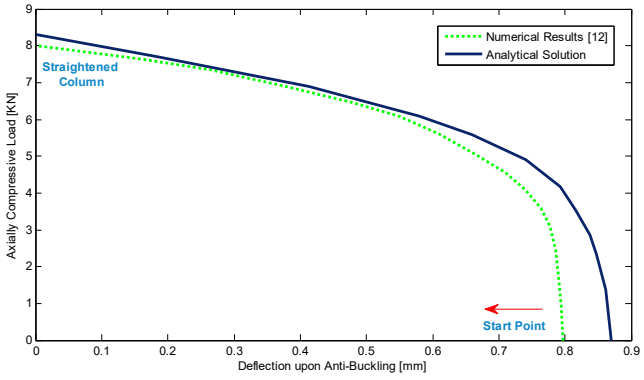

Fig. 12. Analytical solution and numerical results for the relationship between axially compressive load and deflection due to anti-buckling.

Table 6
Material parameters in 1D form for SMA beam-column (Auricchio and Petrini, 2004; Auricchio et al., 2009; Scalet and Peigney, 2017).

Material parameters	Value	Unit
E	53	GPa
E^i	1.46	GPa
R^{1D}	122.5	MPa
ε_L^{1D}	5 %	–
M_s	−34	$^\circ C$
A_f	−13	$^\circ C$

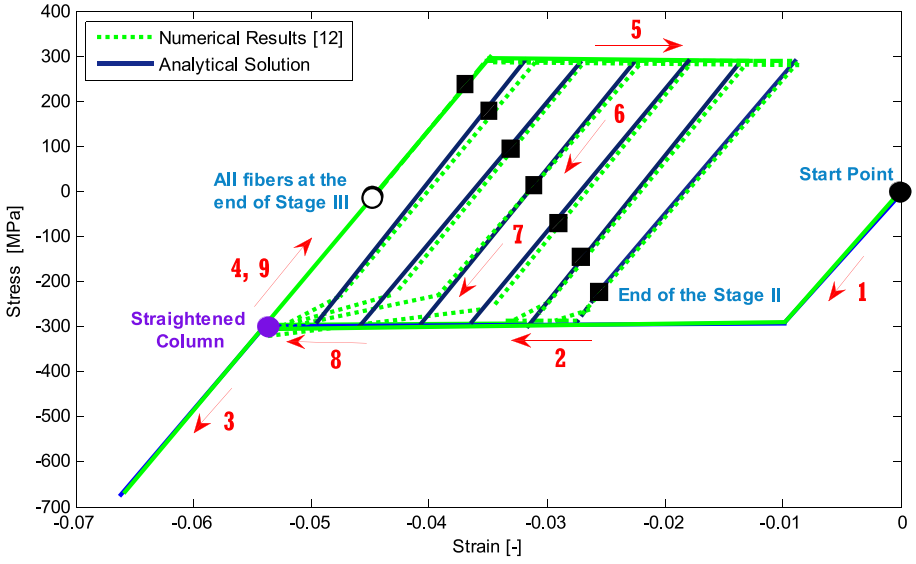

Fig. 10. Stress–strain curves for three different stages at various stages.

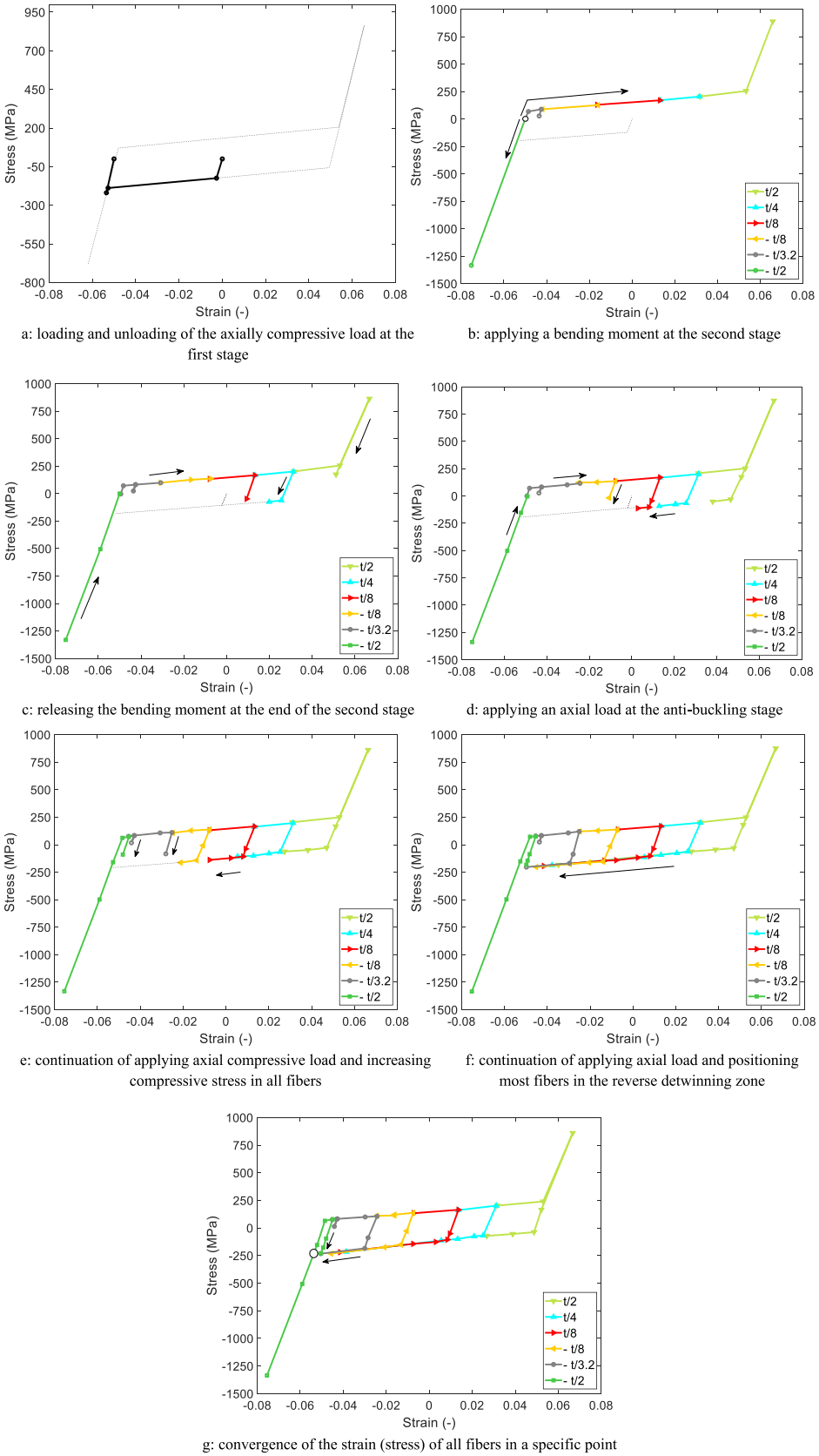

a: loading and unloading of the axially compressive load at the first stage

b: applying a bending moment at the second stage

c: releasing the bending moment at the end of the second stage

d: applying an axial load at the anti-buckling stage

e: continuation of applying axial compressive load and increasing compressive stress in all fibers

f: continuation of applying axial load and positioning most fibers in the reverse detwinning zone

g: convergence of the strain (stress) of all fibers in a specific point

Fig. 13. Variations in stress and strain of some fibers during anti-buckling.

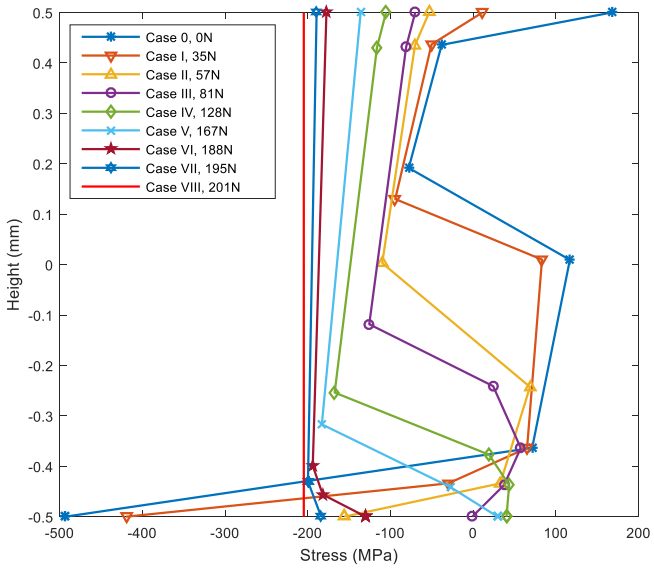

Fig. 14. The trend of changes in the stress distribution across beam cross-section during anti-buckling.

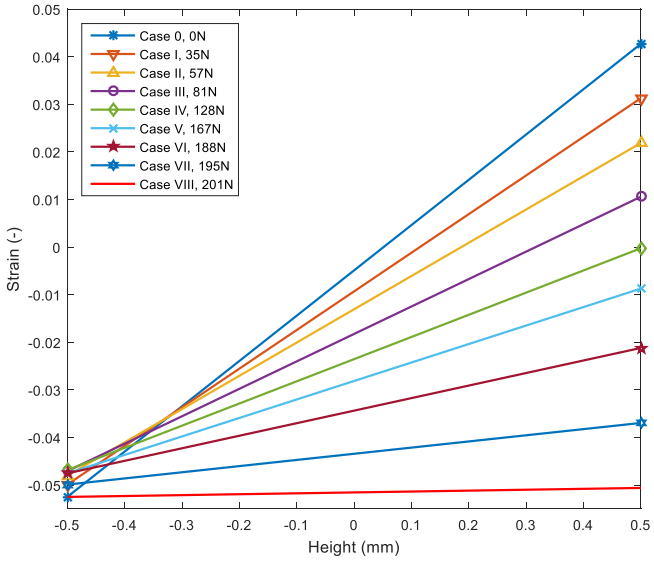

Fig. 15. The trend of changes in the strain distribution across beam cross-section during anti-buckling.

the load they may again reach zero stress.

In the first step, all fibers straightforwardly experience the detwinning process and then stop at zero stress (white bullet ○) upon load relief, arrows 1 to 4 depict this process. In the second step, tensile stress induced by the bending moment causes variant re-orientation (4 to 5), however, an intense compression may be imposed on the fibers on the opposite side (4 to 3). Relieving the moment, stress, and strain for each fiber in tension (5 to 6) seem uniquely demarcated with black squares (■). At the anti-buckling step (7 to 8), as the load is applied, the convergence of strain and stress of column fibers may occur (black bullet) and finally unloading let the axial stress throughout the column reaches zero again (white bullet).

Based on the proposed model, the history of force and deflection variations during anti-buckling are studied incrementally and compared with the results in (Richter et al., 2010). Fig. 11 illustrates the change of transverse displacement along the column length at some specific compressive load; gradually the deflection reduces and finally at about 8

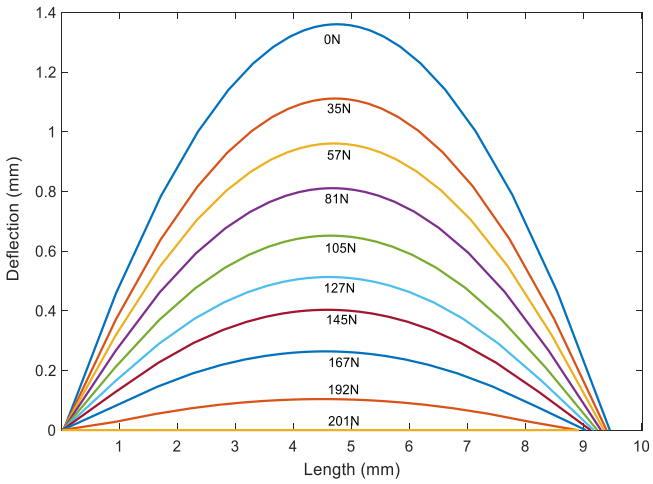

Fig. 16. The trend of changes in deflection along the beam length at different axial loads during anti-buckling.

KN, it is expected to have a straightened column. To figure out the rate of increased compressive load versus reduced transverse displacement, in Fig. 12 we have derived and compared the relationship between axial load versus deflection along the column length. As it is shown, at the initial load increments, the column deflection may not significantly vary, however, when the applied load exceeds 4 KN there is also a corresponding rise in the transverse loading, consequently, at the higher applied loads, a small change in this parameter may lead to a noticeable recovery in the deflection and anti-buckling phenomenon can be seen at a faster speed.

4.2. Example 2

In this example, to proceed more deeply in the anti-buckling behavior and extract all stages of stress distributions in Fig. 5 (a, b), a square beam with a dimension of 1 × 1 mm, length of 10 mm, and material parameters shown in Table 6 are considered. This material behavior was originally experimented by (Sittner et al., 1995) and then adopted and employed in (Auricchio and Petrini, 2004; Auricchio et al., 2009; Scalet and Peigney, 2017). Although it should be noticed that they are in three-dimensional form, thus using Eq. (2), the 1D form has been obtained and represented in Table 6.

For the occurrence of all stages, it is required to induce saturation region in both compression and tension sides of the column. Due to the initial compression of about 210 kN, all fibers will be in the negative saturation region and then the pre-strain reaches −0.058. Subsequently, the length of the beam reduces about 0.5 mm from its initial value, and then upon unloading the stress uniformly comes back to zero (Fig. 13a). By imposing a bending moment of about 90 Nmm, the beam fibers at different positions may follow different paths due to the different amounts of generated strain in each fiber. As shown in Fig. 13 b, the outmost fibers at both sides (−0.5 and 0.5), respectively, might be endured being in negative and positive saturation regions. Moreover, due to the variant re-orientation in tensile sides, some fibers seem to have been loaded in this region (−0.125, 0.125, 0.25). Regarding different moduli of elasticity in saturation and variant orientation regions, there must be a relocation for beam-neutral fiber to satisfy force equilibrium. Thus, the beam is under applied load whereas some fiber similar to −0.3125 strain has an initial loading and then unloading path attributing to the movement neutral fiber. Regarding Fig. 13c, upon unloading the stress could be reduced elastically and/or through variant re-orientation. Once the axial load is applied it is expected to have a stress reduction throughout the beam, however, the compressive side may release its stress and some portions go to the tensile side as illustrated for the fiber at −0.5 mm in Fig. 13d. Given further axial load

gradually causes all fibers to experience negative variant re-orientation (Fig. 13e, f) and eventually in this example both stress and strain of the fibers converge into a specific amount (Fig. 13g), consequently the curvature and deflection return to zero.

The stress distribution diagram in the beam cross-section for all possible stages that can occur during the anti-buckling behavior has been shown in Fig. 14. Stage *0* indicates the residual stress after unloading the bending loads or moment at the second step. After imposing the axially compressive force of about 35 N, the reduced stress from the tensile side is significant and gradually some fibers will be exposed to variant re-orientation. However, on the compression side as we mentioned previously there is a reduction in compressive stress so that some fibers can even experience tensile stress. To discuss in detail, let's consider stage *III* in which almost all fibers that were on the tensile side are now on the compressive side, and in the variant re-orientation region, also some fibers (height of −0.5 to −0.4 mm) that were in the compressive side now have positive stress. From stage *V* onwards more applied compression will cause more fibers come back to the compressive region while the rate of stress changes may not be the same for all fibers. A further continuation in the axial loading leads to a more homogeneous stress distribution across the cross section (stages *VI* and *VII*). Presence of all fibers in a specific point can be seen throughout the beam, so eventually uniform distribution is achieved.

Fig. 15 illustrates the strain variation of all stages corresponding to the stress diagram in Fig. 14. As it is clear strain is changing linearly and eventually in all points of the beam its value is converged into about −0.05. Finally, the beam deflection distribution along the length has been incrementally depicted in Fig. 16 for stages *0* to *VIII*. In each loading increment the amount of transverse deformation is decreased and at the same time, the length shortening of the SMA beam seems to be inevitable.

5. Conclusions

The present paper aims to provide an analytical and experimental investigation into the anti-buckling behavior of prismatic shape memory alloy (SMA) beam-columns. The paper begins by thoroughly describing the process of column straightening during anti-buckling and develops a mathematical model based on this concept. The analytical modeling approach considers nine distinct stages of loading and unloading stages that occur during anti-buckling. Each stage is step by step formulated, and the corresponding force and moment values are derived and presented, primarily for the purpose of designing SMA beam-columns. This step-by-step formulation allows for a detailed representation of the behavior of the beam-columns during anti-buckling. The results show that at different heights along the beam-column, the curvature can be determined based on the inhomogeneous strain distribution. As the axial load increases, the strain distribution across the cross-section of the beam-column becomes more uniform, leading to a reduction in curvature. Eventually, when the strains in all fibers are equalized, the curvature of the beam-column reaches zero, indicating that the structure has been fully straightened under the applied axial load. Therefore, we establish that the primary factor causing the straightening of beam-columns is not the evenness of stress, but rather the achievement of uniformity in strain across all fibers. In Summary:

- This analytical work empowers designers to obtain the required forces and moment in each step based on material parameters and geometry.
- Reverse designing is possible by considering the needed deflection and then calculating the required forces and moments for each step in the present work.
- Material hardening, which is an important parameter in the detwinning process, has been considered in the present work to study anti-buckling behavior.
- Recognition of nine distinct phases depicted on stress-height diagrams, stemming from the intricate stress–strain characteristics exhibited by SMA materials.
- Moreover, when the SMA fibers undergo the saturation region in the second step (bending), we can also discuss the anti-buckling behavior, which makes the model more accurate and comprehensive.

CRediT authorship contribution statement

Alireza Ostadrahimi: Conceptualization, Data curation, Formal analysis, Methodology, Validation, Visualization, Writing – original draft, Writing – review & editing. **Fathollah Taheri-Behrooz:** . **Eunsoo Choi:** Conceptualization, Funding acquisition, Investigation, Methodology. **Guoqiang Li:** Conceptualization, Methodology, Supervision, Writing – review & editing.

Declaration of competing interest

The authors declare that they have no known competing financial interests or personal relationships that could have appeared to influence the work reported in this paper.

Data availability

Data will be made available on request.

Acknowledgement

This work was supported by a grant from the National Research Foundation of Korea (NRF) funded by the Korean government (MEST) (Project No. NRF 2019R1A2C-2008542).

References

Arivanandhan, G., Li, Z., Curtis, S.M., Hanke, L., Quandt, E., Kohl, M., 2023. Power optimization of TiNiHf/Si shape memory microactuators. Actuators 12, 82.
Asadi, H., Bodaghi, M., Shakeri, M., Aghdam, M.M., 2013. On the free vibration of thermally pre/post-buckled shear deformable SMA hybrid composite beams. Aerosp. Sci. Technol. 31, 73–86.
Auricchio, F., Petrini, L., 2004. A three-dimensional model describing stress temperature induced solid phase transformations: solution algorithm and boundary value problems. Int. J. Numer. Meth. Eng. 61, 807–836.
Auricchio, F., Morganti, S., Reali, A., 2009. SMA numerical modeling versus experimental results. In: Proceedings of European Symposium on Martensitic Transformations (ESOMAT 2009), pp. 1–6.
Auricchio, F., Morganti, S., Reali, A., Urbano, M., 2011. Theoretical and experimental study of the shape memory effect of beams in bending conditions. J. Mater. Eng. Perform. 20, 712–718.
Billah, A.H.M.M., Rahman, J., Zhang, Q., 2022. Shape memory alloys (SMAs) for resilient bridges: a state-of-the-art review. Structures 37, 514–527.
Bovesecchi, G., Corasaniti, S., Costanza, G., Tata, M.E., 2019. A novel self-deployable Solar sail system activated by shape memory alloys. Aerospace 6, 78.
Carrera, E., Azzara, R., Daneshkhah, E., Pagani, A., Wu, B., 2021. Buckling and post-buckling of anisotropic flat panels subjected to axial and shear in-plane loadings accounting for classical and refined structural and nonlinear theories. Int. J. Non Linear Mech. 133, 103716.
Cheng, S., Xiao, Y., Li, X., Lin, H., Hua, P., Sheng, L., 2023. Buckling prevention of a single long NiTi tube compressive elastocaloric regenerator. Int. J. Solids Struct. 271–272, 112263.
Choi, E., Ostadrahimi, A., Park, J., 2021. On mechanical properties of NiTi SMA wires prestrained by cold rolling. Smart Mater. Struct. 29, 65009.
Choi, E., Ostadrahimi, A., Lee, Y., Jeon, J.S., Kim, I., 2022. Enabling shape memory effect wires for acting like superelastic wires in terms of showing recentering capacity in mortar beams. Constr. Build. Mater. 319, 126047.
Choi, E., Ostadrahimi, A., Lee, J.H., Jeon, L.S., 2022. On the efficiency of induced prestressing in SMA mortar beams through different thermal stimuli. Smart Mater. Struct. 31 (12), 125026.
Choi, E., Ostadrahimi, A., Kim, W.J., 2022. Enhancement of compressive strength and strain ductility of SMA fiber reinforced concrete considering fiber's aspect ratio. Constr. Build. Mater. 345, 128346.
Das, S., Chakraborty, A., Barua, I., 2021. Optimal tuning of SMA inverter for simultaneous wind induced vibration control of high-rise building and energy Harvesting. Smart Mater. Struct. 30, 025027.
Do, P.T., Le, Q.N., Luong, Q.V., Kim, H.-H., Park, H.-M., Kim, Y.-J., 2023. Tendon-driven gripper with Variable stiffness joint and water-cooled SMA Springs. Actuators 12 (4).

Fahimi, P., Eskandari, A.H., Baghani, M., 2019. A semianalytical solution for bending response of SMA composite beams considering SMA asymmetric behavior. Compos. B Eng. 163, 622–633.
Fang, C., 2022. SMAs for infrastructures in seismic zones: a critical review of latest trends and future needs. J. Build. Eng. 57, 104918.
Hartl, D.J., Mooney, J.T., Lagoudas, D.C., Calkins, F.T., Mabe, J.H., 2010. Use of a Ni60Ti shape memory alloy for active jet engine Chevron application: II. Experimentally validated Numerical analysis. Smart Mater. Struct. 19, 015021.
Havran, J., Psotný, M., 2016. Postbuckling analysis of a rectangular plate loaded in compression. Transactions of the VŠB – Technical University of Ostrava. Civil Eng. Series 15 (2).
Jaber, M.B., Smaoui, H., Terriault, P., 2008. Finite element analysis of a shape memory alloy three-dimensional beam based on a finite strain-description. Smart Mater. Struct. 17, 045005.
Jiang, D., Kyriakides, S., Bechle, N.J., Landis, C.M., 2017. Bending of pseudoelastic NiTi tubes. Int. J. Solids Struct. 124, 192–214.
Karakalas, A., Lagoudas, D., 2020. Effect of tension-compression asymmetry and partial transformation on the response of shape memory alloy beam structures. In: Proceedings of the Behavior and Mechanics of Multifunctional Materials IX, pp. 1–15.
Kawate, S.S., Chethan, K.N., Keni, L.G., Pai, A., Padmaraj, N.H., 2018. Innovations and recent trends in shape memory alloy: a review. Internat. J. Eng. Technol. 7 (4), 2172–2177.
Kazemi, F., Jankowski, R., 2023. Seismic performance evaluation of steel buckling-restrained braced frames including SMA materials. J. Constr. Steel Res. 201, 107750.
Khalid, S., Raouf, I., Khan, A., et al., 2019. A review of human-powered energy harvesting for smart electronics: recent progress and challenges. Int. J. Precis. Eng. Manuf. Green Technol. 6 (4), 821–851.
Kohl, M., 2004. Shape Memory Microactuators. Springer.
Kohl, M., Popp, M., Krevet, B., 2004. Shape memory micromechanisms for microvalve applications. Proc. SPIE 5387, 106–117.
Krishnaswamy, J.A., Buroni, F.C., Garcia-Sanchez, F., et al., 2019. Improving the performance of lead-free piezoelectric composites by using polycrystalline inclusions and tuning the dielectric matrix environment. Smart Mater. Struct. 28 (7), 075032.
Lagoudas, D.C., 2008. Shape Memory Alloys: Modeling and Engineering Applications. Springer.
Li, S., Jia, X., Liu, Z., Ke, L., Yang, J., Kitipornchai, S., 2023. Analysis of bending properties of FG-SMA beam under thermo-mechanical coupling. Int. J. Appl. Mech. 15 (03), 2350016.
Liu, X., He, L., Liu, R., Hu, D., Zhang, L., Cheng, G., 2023. Piezoelectric energy harvesting systems using mechanical tuning techniques. Rev. Sci. Instrum. 94 (3), 031501.
Mandal, P., Calladine, C., 2002. Lateral-torsional buckling of beams and the southwell plot. Int. J. Mech. Sci. 44, 2557–2571.
Mirzaeifar, R., DesRoches, R., Yavari, A., Gall, K., 2013. On superelastic bending of shape memory alloy beams. Int. J. Solids Struct. 50, 1664–1680.
Mohammad Hashemi, Y., Kadkhodaei, M., Sgambitterra, E., Maletta, C., 2023. On the characterization of the compressive response of shape memory alloys using bending. Smart Mater. Struct. 32 (3), 035033.
Ostadrahimi, A., Arghavani, J., Poorasadion, S., 2015. An analytical study on the bending of prismatic SMA beams. Smart Mater. Struct. 24, 125035.
Ostadrahimi, A., Taheri-behrooz, F., 2019. Analytical solution for twinning deformation effect of pre-strained shape memory effect beam-columns. J. Intell. Mater. Syst. Struct. 30, 2147–2165.
Pattar, N., Patil, S.F., 2019. Review on fabrication and mechanical characterization of shape memory alloy hybrid composites. Adv. Compos. Hybrid Mater. 2 (4), 571–585.
Pereira, F. (2016). Plastic Buckling of Columns: Development of a Simplified Model of Analysis.
Qian, H., Zhang, Q., Zhang, X., Deng, E., Gao, J., 2022. Experimental investigation on bending behavior of existing RC beam retrofitted with SMA-ECC composites materials. Materials 15, 12.
Radi, E., 2021. Analytical modeling of the shape memory effect in SMA beams with rectangular cross-section under reversed pure bending. J. Intell. Mater. Syst. Struct. 32 (18–19), 2214–2230.
Rastjoo, S., Fechner, R., Bumke, L., Kötz, M., Quandt, E., Kohl, M., 2020. Development and co-integration of an SMA/Si bimorphnanoactuator for si photonic circuits. Microelectron. Eng. 225, 111257.
Rejzner, J., Lexcellent, C., Raniecki, B., 2002. Pseudoelastic behavior of shape memory alloy beams under pure bending: Experiments and modeling. Int. J. Mech. Sci. 44, 665–686.
Richter, F., Kastner, O., Eggeler, G., 2010. Finite-element simulation of the anti-buckling-effect of a shape memory alloy bar. J. Mater. Eng. Perform. 20, 719–730.
Saeed Kamarian, M., Bodaghi, M., Barbaz Isfahani, R., Song, Jung-il, 2020. A comparison between the effects of shape memory alloys and carbon nanotubes on the thermal buckling of laminated composite beams. Mech. Base. Des. Struct. Mach. 1–24.
Scalet, G., Peigney, M., 2017. A robust and efficient radial return algorithm based on incremental energy minimization for the 3D Souza-Auricchio model for shape memory alloys. Eur. J. Mech. A Solids 61, 364–382.
Shaw, J.A., Kyriakides, S., 1998. Initiation and propagation of localized deformation in elastoplastic strips under uni-axial tension. Int. J. Plast 13, 837–871.
Sittner, P., Hara, Y., Tokuda, M., 1995. Experimental study on the thermoelastic martensitic transformation in shape memory alloy polycrystal induced by combined external forces. Metal. Mater. Trans. 26A, 2923–2935.
Souza, A.C., Mamiya, E., Zouain, N., 1998. Three-dimensional model for solids undergoing stress induced phase transformations. Eur. J. Mech. A Solids 17, 789–806.
Tan, J., Jiang, J., Liu, M., Feng, Q., Zhang, P., Ho, S.C.M., 2019. Implementation of shape memory alloy sponge as energy dissipating material on pounding tuned mass damper: an Experimental investigation. Appl. Sci. 9, 1079.
Thier, M., Mick, A., Drescher, D., Bourauel, C., 1991. Deformation behavior of NiTi shape memory alloys in bending. J. Mater. Sci. 26, 6473–6478.
Tung, H.V., 2017. Thermal buckling and postbuckling behavior of functionally graded carbon-nanotube-reinforced composite plates resting on elastic foundations with tangential-edge restraints. J. Therm. Stresses 40 (5), 641–663.
Urushiyama, Y., Lewinnek, D., Qiu, J., Tani, J., 2003. Buckling of shape memory alloy columns (buckling of curved column and twinning deformation effect). JSME 46, 60–67.
Vahidi, S., Arghavani, J., Choi, E., Ostadrahimi, A., 2021. Mechanical response of single and double-helix SMA wire ropes. Mech. Adv. Mater. Struct. 1–14.
Viet, N., Zaki, W., Umer, R., 2019. Bending theory for laminated composite cantilever beams with multiple embedded shape memory alloy layers. J. Intell. Mater. Syst. Struct. 30, 1549–1568.
Viet, N.V., Zaki, W., Moumni, Z., 2019. A model for shape memory alloy beams accounting for tensile compressive asymmetry. J. Intell. Mater. Syst. Struct. 30, 2697–2715.
Watkins, R.T., Shaw, J.A., 2018. Unbuckling of superelastic shape memory alloy columns. J. Intell. Mater. Syst. Struct. 29, 1360–1378.
Xiao, Y., Jiang, D., 2022. Buckling and unbuckling of Superelastic NiTi tube. Acta Mech. Solida Sin. 35, 647–660.
Zamani Alavije, R., Botshekanan Dehkordi, M., 2019. Nonlinear bending analysis of shape memory alloy beam considering both material and geometric nonlinearity effects. J. Intell. Mater. Syst. Struct. 30, 823–843.
Zhang, X., Feng, P., He, Y., Yu, T., Sun, Q., 2010. Experimental study on rate dependence of macroscopic domain and stress hysteresis in NiTi shape memory alloy strips. Int. J. Mech. Sci. 52, 1660–1670.
Zhou, Y., Stanciulescu, I., Eason, T., Spottswood, M., 2015. Nonlinear elastic buckling and postbuckling analysis of cylindrical panels. Finite Elem. Anal. Des. 96, 41–50.